ORIGINAL PAPER

Deformation characteristics of unstable shallow slopes triggered by rainfall infiltration

Kuo-Hsin Yang[1] · Thanh Son Nguyen[2] · Harianto Rahardjo[3] · Der-Guey Lin[4]

Abstract

Identification of the influence of hydrological and geological factors on slope deformation characteristics (i.e., the displacement–time relationship) under rainfall plays a crucial role in providing early warning information and enabling the implementation of emergency remedial actions before a landslide occurs. In this study, a series of coupled hydro-mechanical finite element analyses were performed to investigate slope displacement behavior triggered by rainfall infiltration. First, the numerical model was validated by comparing the predicted displacement with those measured from a full-scale landslide flume test. A parametric study was then conducted, considering various hydrological conditions and soil hydraulic and mechanical parameters that were statistically determined from a large soil database compiled from relevant literature. Further, the influences of the aforementioned factors on the timing, magnitude, and rate of slope displacement prior to landslide occurrence were quantitatively evaluated in a sensitivity assessment. The numerical results indicated that the slope deformation characteristics could be significantly influenced by various hydrological and geological factors. Nevertheless, the slope displacement over time for all cases generally can be divided into three stages, namely the constant, accelerated, and critical deformation stages, which correspond to various states of slope movement and pore water pressure development. The relationships of slope displacement magnitude and displacement rate with the factor of safety were established, which provide a valuable information in practice for engineers to interpret the slope stability level from a large quantity monitoring data of slope displacement.

Keywords Rainfall-triggered landslides · Early warning system · Coupled hydro-mechanical analysis · Deformation characteristics

✉ Kuo-Hsin Yang
khyang@ntu.edu.tw

Thanh Son Nguyen
sonnt@nuce.edu.vn

Harianto Rahardjo
chrahardjo@ntu.edu.sg

Der-Guey Lin
dglin@dragon.nchu.edu.tw

[1] Department of Civil Engineering, National Taiwan University (NTU), 1, Sec. 4, Roosevelt Rd., Taipei 106, Taiwan

[2] Department of Civil and Construction Engineering, National Taiwan University of Science and Technology (Taiwan Tech), 43, Sec. 4, Keelung Rd., Taipei 106, Taiwan

[3] School of Civil and Environmental Engineering, Nanyang Technological University, 50, Nanyang Avenue, Singapore, Singapore

[4] Department of Soil and Water Conservation, National Chung Hsing University, 145 Xingda Rd, Taichung 402, Taiwan

Introduction

Landslides are major geotechnical disasters that occur worldwide. Rainfall-induced shallow landslides are the most frequently reported causative factor of landslides, and their frequency of occurrence is increasing rapidly because of extreme rainfall events caused by global warming and climate change. According to the United States Geological Survey (USGS), shallow landslides, classified as translational earth slides, predominately occur in areas covered by a residual or colluvium soil deposit underlain by less permeable rock. The failure plane is approximately parallel to the slope surface, with the failure depth typically ranging from 1 to 3 m (Caine 1980; Johnson and Sitar 1990; Fourie et al. 1999; van Asch et al. 1999; Tohari et al. 2007; Trandafir et al. 2008; Wesley 2011; Bordoni et al. 2015; Chae et al. 2015; Kim and Song 2015; Oh and Lu 2015; Zhang et al. 2017).

Numerous studies have been conducted on the hydrological response and failure mechanism of rainfall-induced

shallow landslides by using various approaches, such as model tests (Wang and Sassa 2001, 2003; Tohari et al. 2007; Gallage et al. 2012; Chae and Kim 2012; Chen et al. 2012; Hakro and Harahap 2015; Chinkulkijniwat et al. 2016; Lora et al. 2016; Montoya-Domínguez et al. 2016; Park 2016; Ahmadi-Adli et al. 2017; Regmi et al. 2017; Sasahara 2017; Wu et al. 2015, 2017; Fan et al. 2018; Kim et al. 2018; Cogan and Gratchev 2019; Jing et al. 2019; Zhang et al. 2019), centrifuge tests (Wang et al. 2010; Zhang et al. 2011; Bhattacherjee and Viswanadham 2017), case study and field monitoring (Gasmo et al. 1999; Zhang et al. 2000; Okura et al. 2002; Moriwaki et al. 2004; Ochiai et al. 2004; Li et al. 2005; Rahardjo et al. 2005; Trandafir et al. 2008), and numerical analyses (Casagli et al. 2005; Ye et al. 2005; Leung and Ng 2013; Leshchinsky et al. 2015; Qi and Vanapalli 2015; Bandara et al. 2016; Suradi et al. 2016; Yang et al. 2017; Yubonchit et al. 2017; Wang et al. 2018; Tang et al. 2019). These studies have revealed that the soil volumetric water content (VWC) and pore water pressure (PWP) exhibit spatiotemporal variation within slopes subject to wetting and drying cycles. The failure mechanisms of rainfall-induced shallow landslides primarily involve the advancement of the wetting front, which causes increased PWP (loss of suction or development of positive PWP) within the soils. An increase in the PWP leads to a decrease in the soil shear strength, which results in slope failure. Slope stability is directly influenced by PWP variation, which is a function of the rainfall intensity, infiltration rate, soil's saturated and unsaturated hydraulic properties, and slope geometry.

Many of the aforementioned studies focused on assessing the hydrological response (i.e., the variation of water content and PWP within soils) and stability (i.e., the factor of safety, FS) of a shallow slope subjected to rainfall. The relationship of rainfall intensity and duration with landslide occurrence has also been evaluated in past studies to establish rainfall thresholds above which a landslide could be triggered. However, few attempts have been made to investigate the deformation characteristics (i.e., displacement–time relationship) of slopes subjected to rainfall (Alonso et al. 2003; Zhou et al. 2009; Leung and Ng 2016; Yang et al. 2017; Tang et al. 2019). The reason for few studies on this subject is that assessment of slope displacement is a complex coupled hydro-mechanical problem that involves a change in the soil's mechanical and hydraulic properties as the soil transits from unsaturated to saturated conditions, and the water table varies with time as rainfall continues (Lee et al. 2011).

The importance of understanding slope deformation characteristics under rainfall is twofold. First, in practical landslide risk management, a single slope displacement criterion is adopted for all slopes in the early warning system regardless of whether slopes have different hydrological and geological conditions. Investigation of slope deformation characteristics, particularly the evaluation of the influence of hydrological

conditions and soil mechanical and hydraulic parameters on slope displacement under rainfall, could provide useful insights for developing a slope displacement criterion with customized values for slopes under different conditions. Second, in current practice, the stability of a slope is often interpreted from the slope displacement obtained using inclinometer readings or satellite image interpretation. However, a missing link exists between the monitored slope displacement information and corresponding soil stress state and stability level of the investigated slope. Further research on slope deformation characteristics is required to establish the relationships between slope displacement (e.g., magnitude or rate) and slope stability levels (e.g., FS).

The aforementioned discussion motivated the authors of this paper to conduct a series of coupled hydro-mechanical finite element (FE) analyses to investigate slope deformation behavior of slopes triggered by rainfall. The framework of unsaturated soil mechanics was incorporated into simulations to model the mechanical and hydraulic responses of soils during rainfall. The objectives of this study were as follows: (1) to validate the applicability of the proposed numerical model in predicting a slope's hydraulic response and deformation, (2) to examine the mechanism that triggers slope deformation and the process of slope displacement over time, (3) to evaluate the influence of hydrological conditions and soil mechanical and hydraulic parameters on slope displacement, and (4) to establish the relationships of slope displacement magnitude and displacement rate (velocity) with the FS. On the basis of the findings, practical implications and suggestions regarding landslide warnings based on slope surface displacement and displacement rate are discussed.

Theoretical framework and model validation

Numerical model and procedure

A full-scale landslide flume test (Fig. 1a) performed by Moriwaki et al. (2004) was used to validate the applicability of the proposed numerical model in predicting a slope's hydraulic response and deformation. The model slope in the landslide flume test was 23 m long, 7.8 m high, 3 m wide, and 1.2 m deep and consisted of three parts: an upper 30° slope segment, a lower 10° slope segment, and a horizontal segment at the toe of the model slope. The slope was constructed using loose Sakuragawa River sand, which is classified as poorly graded sand (SP) according to the Unified Soil Classification System (USCS). Instruments were installed along the slope (Fig. 1b) to measure the development of slope displacement and PWP during rainfall. A constant rainfall of intensity 100 mm/h was applied to the slope. The slope began to deform at 113 min after commencement of the rainfall, after which the displacement increased continuously (prefailure

Fig. 1 Model slope for numerical model validation: **a** physical test (landslide flume test by Moriwaki et al. 2004) and **b** numerical model and configuration of instrumentation
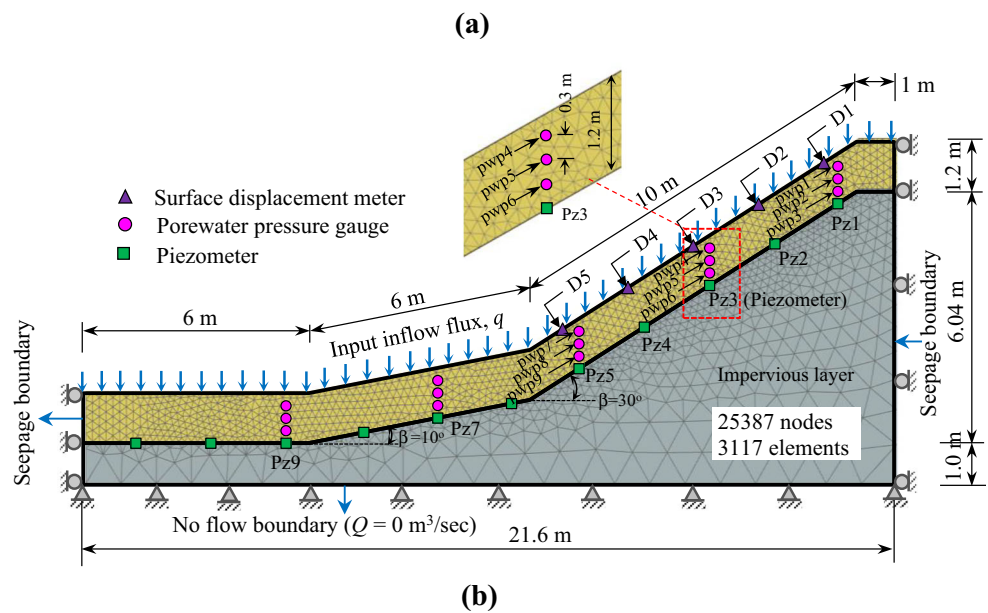
stage). A rapid landslide occurred at 154 min (failure stage). The collapsed soil mass slid downward and deposited in a final position within approximately 5 s (postfailure stage). Detailed information on the test setup and experimental results can be found in Moriwaki et al. (2004).

In the present study, a series of fully coupled hydromechanical analyses were performed using the FE program PLAXIS (Brinkgreve et al. 2019) to simultaneously analyze PWP variation and slope displacement within the slope. Figure 1b shows the numerical model used for validation. The FE meshes with 15-node triangular elements of the entire numerical model consisted of 25,387 nodes and 3117 elements, and the FE meshes of the surface soil layers were refined to generate a high degree of freedom for the slope system to predict surface displacement. Standard fixities were specified for the mechanical boundary conditions: a roller for the two side boundaries and a hinge for the bottom boundary. As for the hydraulic boundary conditions, zero flux was

assigned along the bottom boundary, and the seepage boundary was imposed along both the right and left boundaries to allow the free flow of seepage water (Fig. 1b). The numerical simulation was performed in two steps: generation of the initial condition and implementation of the rainfall. Transient seepage analysis was first conducted with small unit flux on the slope surface to generate a uniform PWP distribution of -7 kPa, which was estimated from the initial water content of the soil in the test. On the generation of the initial condition, inflow flux of $q = 100$ mm/h, which is equal to the rainfall intensity in the test, was applied to the slope surface for a period of time ($t = 9267$ s) until slope failure occurred.

Soil parameters

In this study, the hydraulic and mechanical behavior of unsaturated soil under rainfall infiltration conditions is described using the framework of unsaturated soil mechanics. The van

Genuchten–Mualem model (van Genuchten 1980; Mualem 1976) was used to simulate the infiltration and transient seepage behaviors of unsaturated soil under rainfall condition. The soil–water characteristic curve (SWCC) and soil hydraulic conductivity function (HCF) are expressed in Eq. 1 and Eqs. 2 and 3, respectively.

$$\theta = \theta_r + (\theta_s - \theta_r)[1 + \{\alpha(u_a - u_w)\}^n]^{1/n-1} \tag{1}$$

where θ = volumetric water content; θ_s and θ_r = saturated and residual volumetric water content, respectively; α = fitting parameter related to air entry value; n = fitting parameter related to the gradient of the curve; and $(u_a - u_w)$ = matric suction (where u_a and u_w are the pore air and pore water pressures, respectively).

$$k_{rel} = \frac{k}{k_s} = \Theta^{1/2} \left[1 - \left(1 - \Theta^{1/(1-1/n)}\right)^{1-1/n}\right]^2 \tag{2}$$

$$\Theta = \frac{\theta - \theta_r}{\theta_s - \theta_r} \tag{3}$$

where Θ = normalized volumetric water content, k_{rel} = relative hydraulic conductivity, k = hydraulic conductivity at a given pore water pressure, and k_s = saturated hydraulic conductivity.

Figure 2 displays the SWCC and HCF of the test soil used for the numerical model validation. Table 1 summarizes the van Genuchten–Mualem model parameters for the test soil. The SWCC was first estimated using the predictive method proposed by Houston et al. (2006) based on the soil grain-size distribution and index properties. The van Genuchten–Mualem model presented in Eq. 1 was then used to determine the fitting parameters α and n of the SWCC. Finally, the van Genuchten–Mualem model presented in Eq. 2 with the determined fitting parameters was employed to predict the HCF of the test soil. As depicted in Fig. 2a, the SWCC of the test soil (Sakuragawa River sand) falls in the typical range for sandy soil suggested by Griffiths and Lu (2005). The k_s value of the test soil required for HCF was estimated using various empirical methods (Hazen 1892; Kozeny 1927; Slichter 1954; Beyer 1964) and ranged from 4.6×10^{-5} to 3.0×10^{-4} m/s. By comparing the predicted timings of slope failure, the k_s value for the best-fitted result was determined to be 3.0×10^{-4} m/s. This value is consistent with the typical range suggested by Griffiths and Lu (2005) for the k_s value of sandy soil.

In PLAXIS, the soil effective stress under unsaturated conditions was defined using Bishop's equation (Bishop 1954, 1959) as follows:

$$\sigma' = (\sigma - u_a) + \chi(u_a - u_w) \tag{4}$$

where σ' and σ = effective and total stress, respectively; $\sigma - u_a$ = net normal stress; and χ = soil parameter in the range of 0 to

1. In PLAXIS, χ is assumed to equal the effective saturation S_e, which is expressed as follows:

$$S_e = \frac{S - S_r}{S_s - S_r} \tag{5}$$

where S = degree of saturation and S_s and S_r = degree of saturation at the fully saturated state (= 100%) and at the residual state, respectively. Notably, $S_e = \Theta$, which can be derived numerically according to the soil's weight–volume relationship. When soil is saturated ($S_e = 1$), Eq. 4 becomes $\sigma' = \sigma - u_w$, which coincides with Terzaghi's effective stress for saturated soil. Thus, a smooth transition occurs between the saturated and unsaturated states.

The extended Mohr–Coulomb failure criterion proposed by Vanapalli et al. (1996) was used to calculate the unsaturated soil shear strength as follows:

$$\tau = c' + (\sigma_n - u_a)\tan\varphi' + \Theta\left[(u_a - u_w)\tan\varphi'\right] \tag{6}$$

where τ = soil shear strength, c' = effective cohesion, ϕ' = effective friction angle, and the rest of the parameters have been defined previously. Equation 6 describes the nonlinear relationship between soil strength and suction and provides realistic modeling of soil shear strength when soil is partially unsaturated (Zhang et al. 2014). When soil is saturated ($\Theta = 1$), Eq. 6 becomes equivalent to the conventional Mohr–Coulomb failure criterion.

The hardening soil (HS) model, an elastoplastic soil constitutive model, was used for the simulation of soil behavior. The HS model has a nonlinear (hyperbolic) and stress-dependent modulus, which is defined as follows:

$$E_{50} = E_{50}^{ref} \left(\frac{\sigma_3' + c'\cot\phi'}{p^{ref} + c'\cot\phi'}\right)^m \tag{7}$$

where E_{50} = secant modulus corresponding to 50% of stress level, E_{50}^{ref} = reference stiffness modulus corresponding to the reference confining pressure p^{ref}, σ_3' = the effective lateral pressure at the mid-depth of the soil layer, p^{ref} = reference confining pressure (= 1 atm = 101.3 kPa), and m = exponential power. The nonlinear soil stress–strain relation in the HS model can effectively model the changes in soil modulus at different stress levels and thus appropriately simulate soil deformation under large soil strain conditions. Furthermore, the stress-dependent modulus in the HS model is an essential feature for appropriately describing changes in the soil modulus with matric suction to model the unsaturated soil behavior.

Table 1 lists the input soil mechanical properties used in the numerical model validation. The soil properties for Sakuragawa River sand were adopted from Moriwaki et al. (2004) and Ghasemi et al. (2019). The sand behavior was

Fig. 2 Hydraulic characteristic curves of Sakuragawa sand in the landslide flume test: **a** SWCC and **b** HCF

(a)

(b)
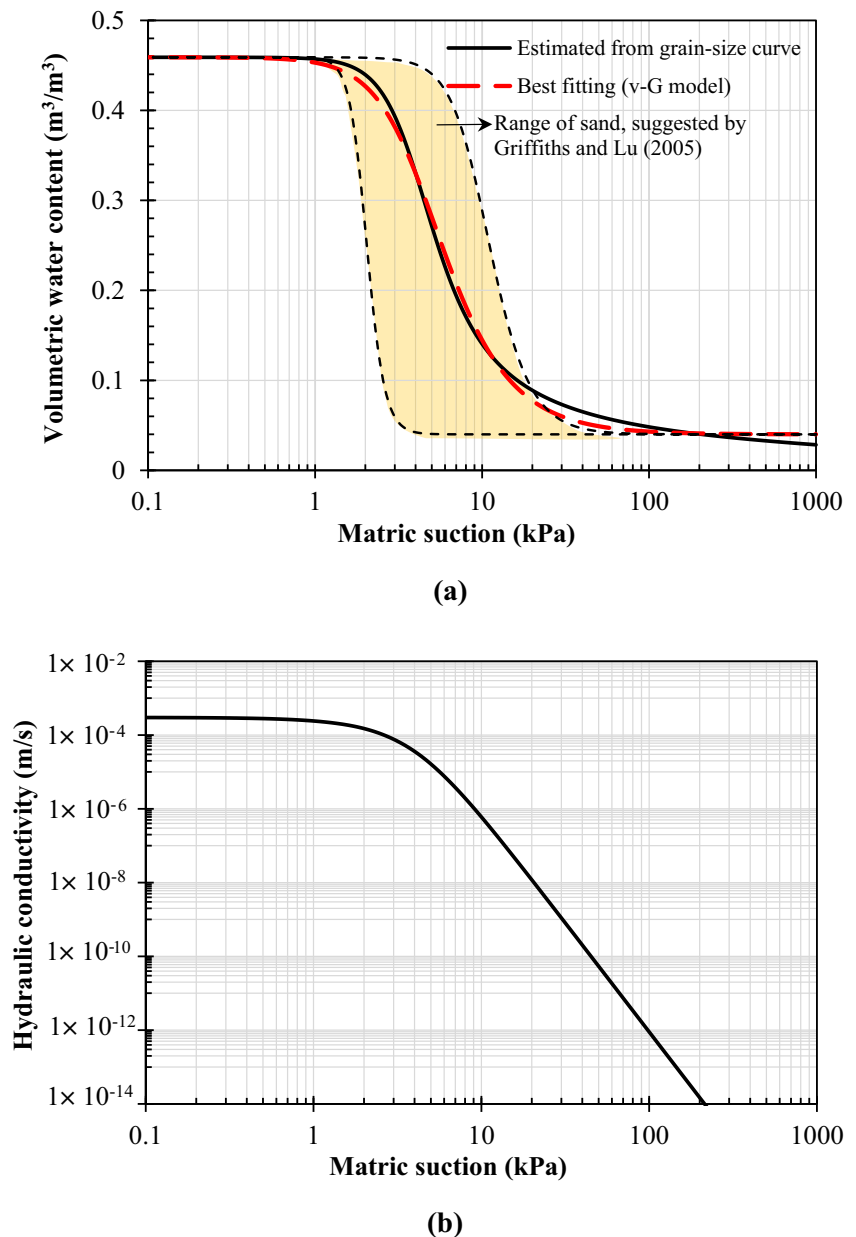
analyzed using effective stress parameters under drained conditions. The steel flume was modeled as an impervious bedrock layer underlying the sand layer. The bedrock layer was modeled using a nonporous and linear elastic material with a relative high Young's modulus to ensure that it behaved as a rigid material (Camera et al. 2014).

Results and comparison

The numerical model was verified by comparing the level of the phreatic surface, the location of the failure surface, ground surface displacements, and failure timing of prediction with those of measurement. This validation focused only on the prefailure and failure stages. The postfailure stage was not evaluated in this study because of the limitation of FE formulation in modeling large soil deformation, which could cause the distortion of FE meshes and the consequent numerical illness. Figure 3a presents a comparison of the measured level of the phreatic surface immediately before slope failure with the predicted level of the zero PWP surface. Figure 3b illustrates a comparison of the measured location of the failure surface with the predicted location comprised of the plastic points. The measurements and predictions are generally in favorable agreement. Both the landslide flume test and numerical simulation indicated that slope failure was initiated in the upper 30° slope segment.

Table 1 Input soil properties for numerical model validation and baseline case

Soil model parameters	Symbol	Model validation	Baseline case	
		Sand	Soil layer	Bedrock
Mechanical parameters				
Soil model		HS	HS	MC
Analysis type		Unsaturated drained	Unsaturated drained	Saturated undrained
Dry unit weight (kN/m³)	γ_{unsat}	15.7	16	24
Saturated unit weight (kN/m³)	γ_{sat}	19.1	18.1	24
Cohesion (kPa)	c' or S_u	0.1	7.0	500
Friction angle (°)	ϕ'	34	31.5	0
Dilatancy angle (°)	ψ	4[a]	1.5[a]	–
Secant modulus (kPa)	E_{50}^{ref} or E_u	10,000	15,000	876×10^5
Primary oedometer loading modulus (kPa)	E_{oed}^{ref}	10,000[b]	10,500[b]	–
Unloading/reloading modulus (kPa)	E_{ur}^{ref}	30,000[c]	45,000[c]	–
Modulus exponent	m	0.5	0.5	–
Poisson's ratio	υ_{ur} or υ	0.3	0.3	0.495
Failure ratio	R_f	0.9	0.9	–
Hydraulic parameters				
Saturated hydraulic conductivity (m/s)	k_s	3×10^{-4}	3×10^{-5}	1×10^{-13}
Saturated volumetric water content	θ_s	0.459	0.445	–
Residual volumetric water content	θ_r	0.040	0.108	–
Fitting parameter (kPa⁻¹)	α	0.23	0.25	–
Fitting parameter	n	2.56	1.70	–

[a] Estimated by $\psi = \phi' - 30°$ (Bolton 1986)

[b] Assume to be E_{50}^{ref} for sand and $0.7 E_{50}^{ref}$ for soil layer

[c] Assume to be $3 E_{50}^{ref}$ as the default value in PLAXIS

The failure surface developed along the soil–bedrock interface at the upper slope, which resulted in a translational slide failure.

Figure 4 displays the measured and predicted surface displacement with time at three selected locations (D1, D3, and D5 in Fig. 1) along the slope surface. The displacement trends of prediction well coincide with those of measurement for all three locations. For both the measurements and predictions, the slope starts to move after $t = 6700$ s, which corresponds to the time required for the wetting front to reach the base of the soil and the soil becomes saturated at the soil–bedrock interface. The slope displacement approximates 50 mm at the inception of slope failure (FS = 1.0) for both prediction and measurement, and the failure timing of prediction ($t = 9300$ s) also closely matches that of measurement ($t = 9267$ s).

In summary, good agreement can be achieved between the measurements and predictions in many aspects. The model validation results indicate that the fully coupled hydromechanical model used in this study can capture the mechanical and hydraulic response as well as the deformation characteristics of shallow slopes subjected to rainfall. Subsequently, the proposed numerical model was adopted to investigate the slope deformation characteristics under rainfall as described in the following sections.
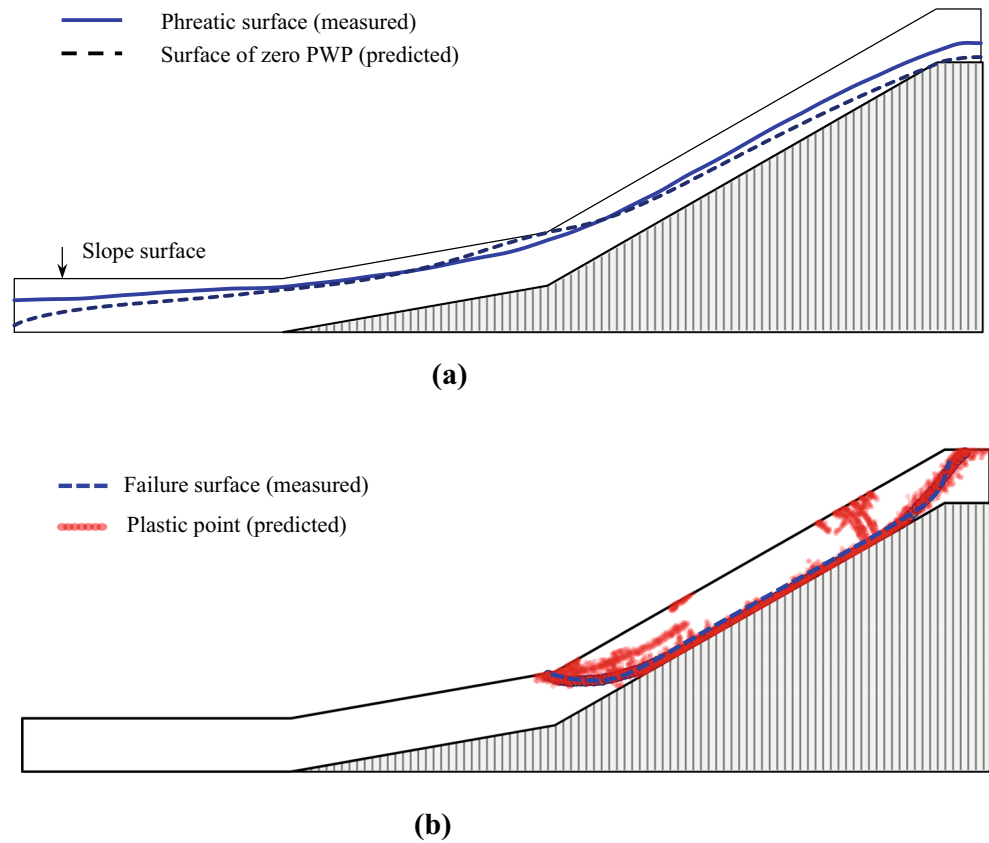
Numerical modeling

Landslide database

A database of 57 soil types was compiled from 35 landslide case histories of the literature and listed in Table 6 in the Appendix. The datasets cover a wide range of soil types, including residual weathered soils and transported colluvium deposits worldwide. Figure 5 displays the probability density functions of the various soil hydraulic and mechanical parameters, and Fig. 6 depicts the variation in the SWCC and HCF of the soils for the numerical evaluation in this study. Table 2 summarizes the statistical attributes of the soil dataset (i.e., maximum and minimum value, mean, and standard deviation, SD) calculated from the probability density functions displayed in Fig. 5. The mean values of soil properties were input to the baseline case in the numerical simulation, and the values bounded by maximum and minimum values were used in the parametric study, as discussed later.

Numerical model

An FE slope model was established to model a shallow slope with total length of 120 m and slope angle of 30° (Fig. 7). The

Fig. 3 Model validation by comparing the location of **a** phreatic surface and **b** failure surface

Phreatic surface (measured)

Surface of zero PWP (predicted)

Slope surface

(a)

Failure surface (measured)

Plastic point (predicted)

(b)

slope model comprised a 3-m-thick soil layer underlain by an impermeable rock layer. The value of the thickness of the soil layer was determined based on the collected landslide database presented in Table 6 in the Appendix. More than 80% of the landslide cases in the collected landslide database have soil

thickness ranging from 1 to 5 m. Based on the above statistical results, a 3-m-thick soil layer, the average value of 1–5 m, was selected in this study. The ratio of slope length to soil thickness in the slope model (L/H) was 30, which is larger than the suggested value (= 25) to ensure no interference from

Fig. 4 Model validation by comparing the surface displacement and failure timing

FS = 1.35 FS$_{cr}$ = 1.1 FS = 1

Constant Accelerated Critical

$v < 1$ mm/h $v > 38$ mm/h

failure at t_f = 9300 s

Characteristics	Predicted	Measured
Surface displacement	—○— D1	----- D1
	—□— D3	—— D3
	—△— D5	— — D5
Failure timing	9300 s	9267 s

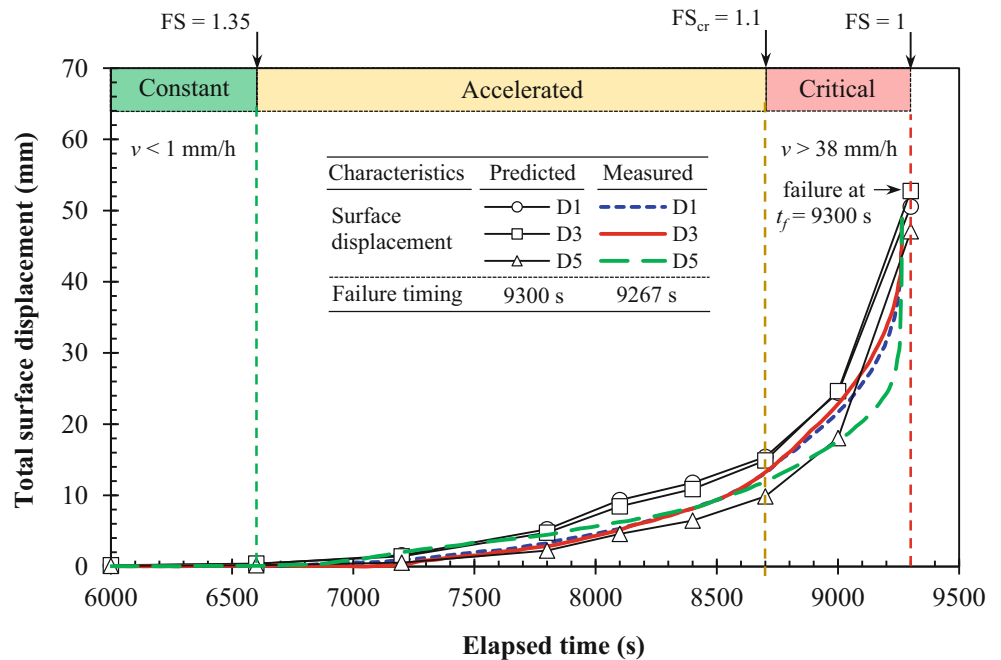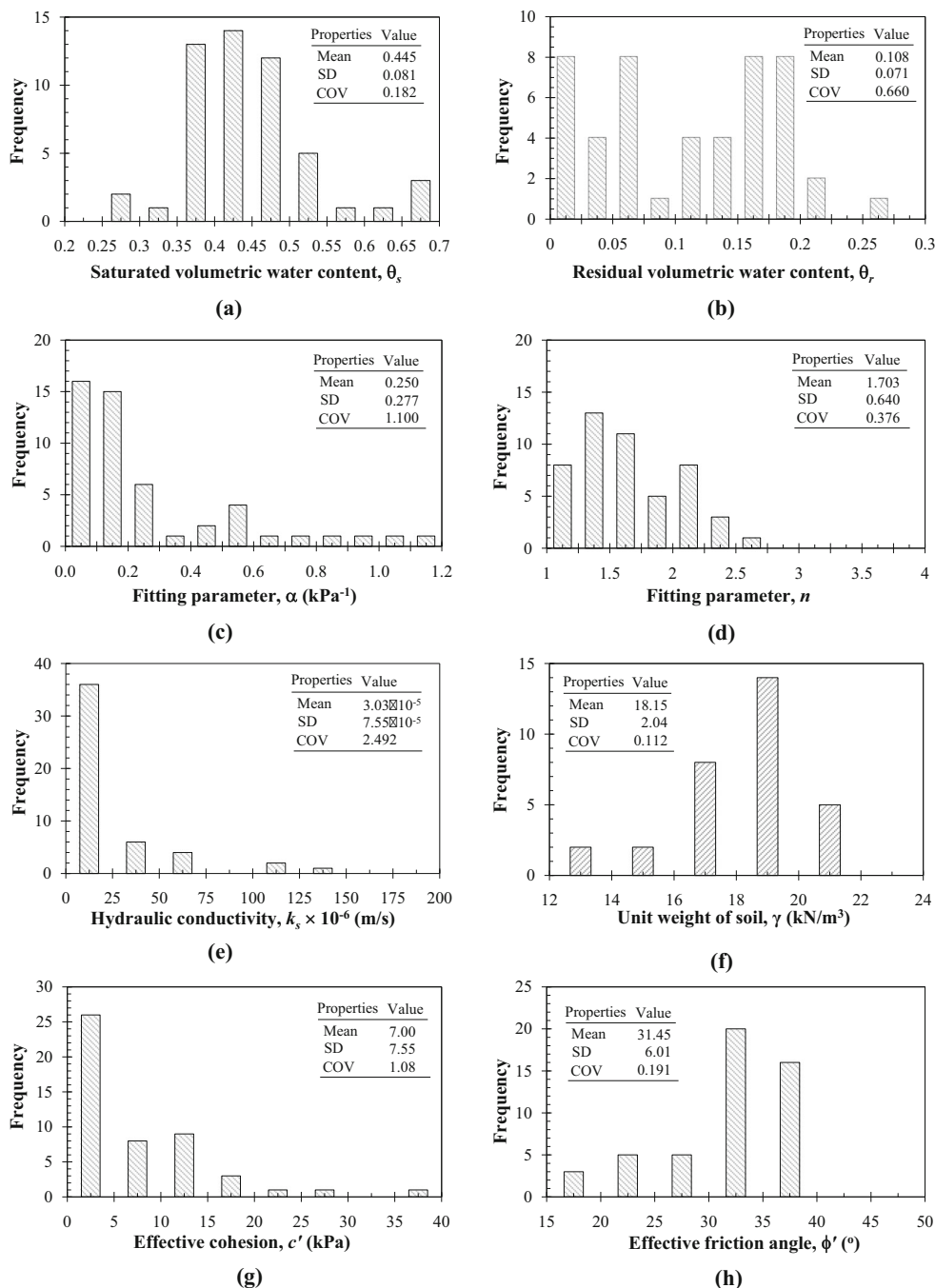Total surface displacement (mm)

Elapsed time (s)

Fig. 5 Probability density functions of various soil parameters: **a** saturated volumetric water content; **b** residual volumetric water content; **c, d** fitting parameter α and n, respectively; **e** saturated hydraulic conductivity; **f** unit weight of soil; **g** effective cohesion; **h** effective friction angle


boundaries in the calculation of slope deformation (Griffiths et al. 2011; Milledge et al. 2012).

The soil was modeled using the HS model, and the soil behavior was analyzed using effective stress parameters under drained conditions. The bedrock was modeled using the Mohr–Coulomb model with a high Young's modulus to ensure that the bedrock deformation was negligible. The FE mesh with 15-node triangular elements consisted of 32,261 nodes and 3968 elements (Fig. 7). The element sizes were refined (i.e., element global height of 0.2 m) in the soil layer, where large deformation and PWP variation are expected to

occur. Sections A, B, and C—in the upper, middle, and lower parts of the slope, respectively—were selected to present the numerical results.

The boundary conditions and numerical procedure were the same as those used in the validation model, except that the values of inflow flux q were input differently on the basis of the selected rainfall intensity. The FS of the slope was calculated using the phi/c strength reduction method in PLAXIS. All simulations were terminated at the critical state of slope failure (FS = 1). During the calculation, each step/phase of coupled analyses was followed by an additional

Fig. 6 Hydraulic characteristic curves of soils collected from the literature: **a** SWCC and **b** HCF

(a)

(b)
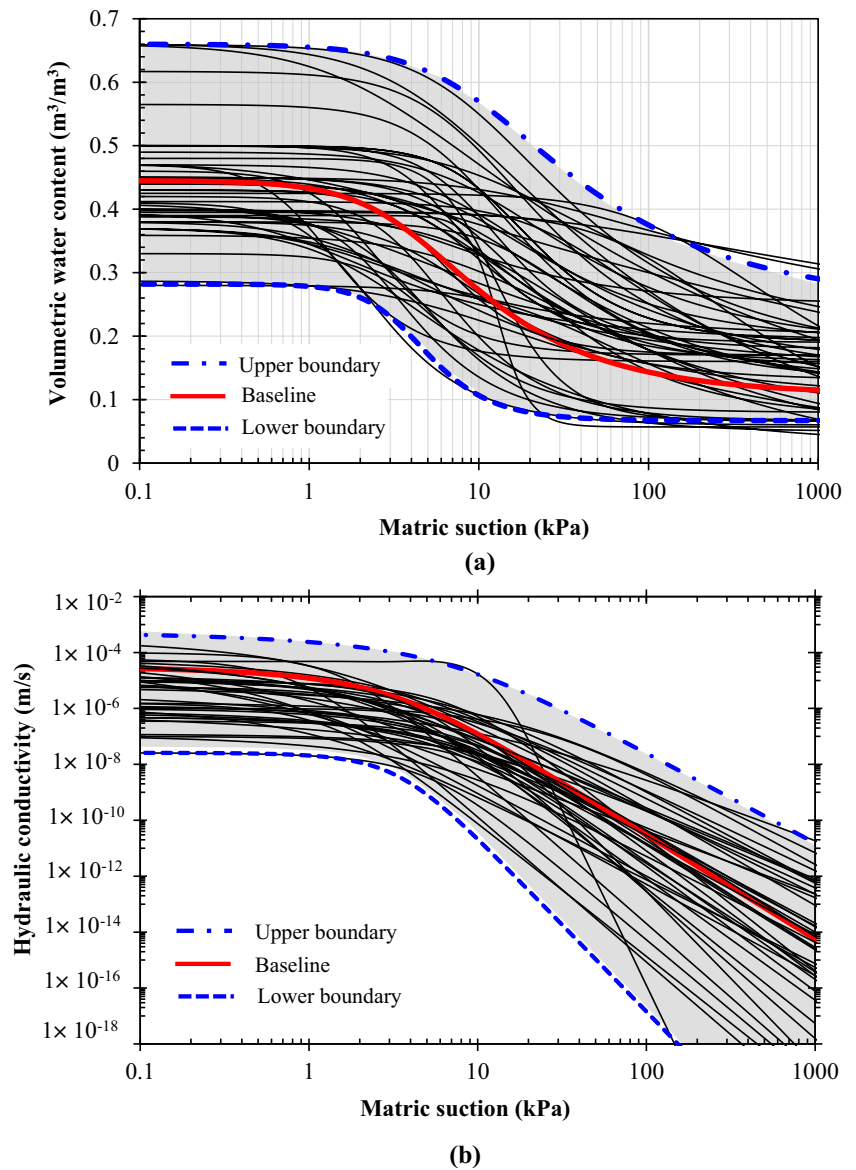
step of phi/c reduction analyses. Therefore, the FS value can be evaluated at different steps/times during the entire calculation process. However, the values of slope displacement were obtained from the coupled analyses and not from the phi/c reduction analyses.

Implementation of numerical analyses

The numerical analyses were performed in two series: a baseline case and parametric study. Totally, 26 cases of numerical simulations have been carried out in this study (Table 3).

Table 2 Summary of the statistical attributes of the compiled soil dataset

Parameters	Soil type	Hydraulic parameter					Mechanical parameter		
	USCS	θ_s	θ_r	α (kPa^{-1})	n	k_s (m/s)	γ (kN/m^3)	c' (kPa)	ϕ' (°)
Number of data	57	51	47	50	50	51	31	49	49
Maximum value	SM, SC, SW, MH-CL,	0.660	0.250	1.200	5.239	5.0×10^{-4}	21.6	35.8	39.5
Minimum value	MH-ML, CL	0.282	0	0.007	1.092	2.6×10^{-8}	13.1	0	17
Mean, μ		0.445	0.108	0.250	1.703	3.0×10^{-5}	18.1	7.0	31.5
Standard deviation, SD		0.081	0.071	0.277	0.640	7.5×10^{-5}	2.04	7.6	6.0
Coefficient of variation, COV %		18.2	65.7	110.8	37.6	249.2	11.2	108	19.1

Fig. 7 Geometric dimensioning and layout of investigation points for model shallow slope
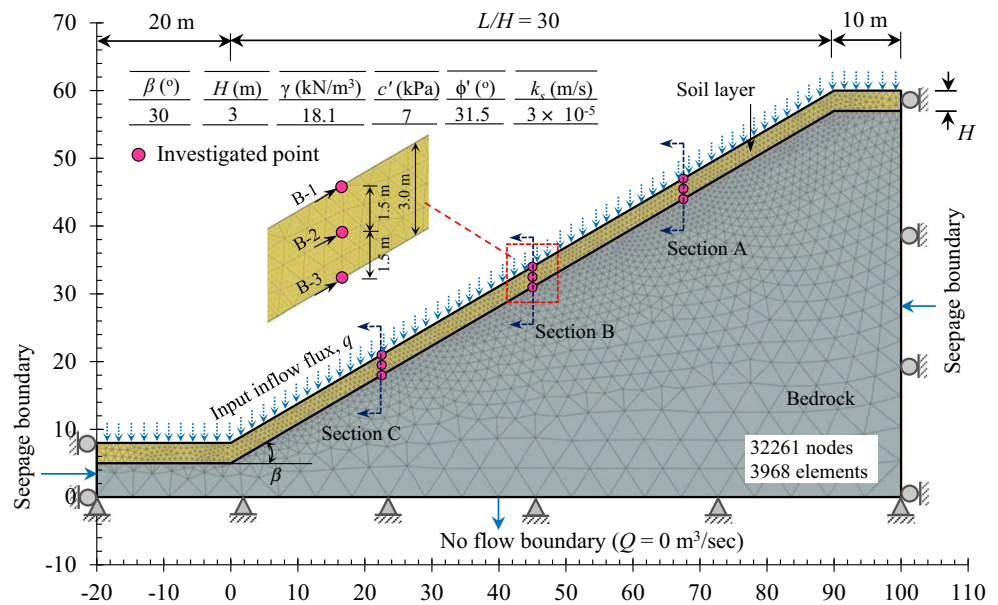
Notably, different input soil properties were used in the baseline case and parametric study because the two series of analyses served different purposes. The input soil parameters listed in Tables 1 and 3 and used for the baseline case were obtained from the mean values of the soil properties of the compiled dataset in Table 2. Moreover, according to the soil modulus value suggested by Rahardjo et al. (2011) and Yang et al. (2017) from actual landslide cases, E_{50}^{ref} was assumed to be 15,000 kPa, which results in an E_{50} value of 6780 kPa at the mid-depth of the soil layer. The sensitivity of the soil modulus to slope deformation was evaluated in the parametric study.

In the baseline case, an initial suction of $\psi_0 = 10$ kPa was first generated and then a rainfall intensity of $I = 16.25$ mm/h (or 390 mm/day) was applied to the upper surface of the slope. This I value was referenced from Chen et al. (2015) based on the rainfall data which caused 263 cases of landslide disasters in Taiwan. The ratio of rainfall intensity to soil saturated hydraulic conductivity (I/k_s) was 0.15. An I/k_s value < 1 indicates that the inflow flux (i.e., I) is less than the outflow flux (limited by the k_s value of the soil). Thus, all the rainwater can infiltrate the soil and no run-off occurs in the baseline model. The effect of rainfall intensity on slope deformation characteristics was also examined in the parametric study.

In the parametric study, the input parameters were divided into three main groups (Table 3): hydrological conditions (i.e., initial conditions and rainfall intensity), soil hydraulic parameters (i.e., saturated hydraulic conductivity, SWCCs, and HCFs), and soil mechanical parameters (i.e., unit weight, friction angle, cohesion, soil modulus, and dilatancy). The effects of these parameters on slope displacement were evaluated. In each case, only one parameter was varied, with all other parameters kept the same as those in the baseline case. Regarding the input soil properties, the soil property values within one SD of the mean

($\mu \pm$ SD) were selected in the parametric study. If $\mu -$ SD was negative or unreasonable, the minimum value of the parameter in Table 2 was used as the lower bound. The SWCC and HCF are governed by three parameters (n, α, and k_s in Eqs. 1 and 2). For data visualization, Fig. 8 illustrates the input soil hydraulic characteristic curves obtained by individually varying the values of n, α, and k_s.

Regarding the input hydrological conditions, three initial suction values ($\psi_0 = 5$, 10, and 20 kPa) were adopted in the parametric study. These values were selected on the basis of field measurement values of landslide slopes reported in the literature (Cuomo and Della Sala 2013; Sorbino and Nicotera 2013; Song et al. 2016; Tofani et al. 2017). Notably, the initial suction value was influenced by the antecedent hydrological conditions. Higher suction can possibly develop in the field under a prolonged drought; however, the evaluation of this extreme condition was beyond the scope of the present study. In addition, five rainfall intensities, which were normalized by k_s, were selected in the parametric study: $I/k_s = 0.02$ ($I = 2.16$ mm/h) and 0.05 ($I = 5.4$ mm/h) for light rainfall, 0.15 ($I = 16.2$ mm/h) for moderate rainfall, 0.3 ($I = 32.4$ mm/h) for heavy rainfall, and 0.5 ($I = 54$ mm/h) for extremely heavy rainfall. These intensities were selected in accordance with the rainfall classification system of the Taiwan Central Weather Bureau.

Results and discussion

Baseline case

In the baseline case, the hydraulic response of the slope, the triggering mechanism of slope deformation, and the process of slope displacement over time were examined. Figure 9

Table 3 Cases of numerical simulations and input parameters

Series of analyses	Hydrological conditions		Hydraulic parameters			Mechanical parameters				
	Initial suction	Rainfall intensity	Saturated hydraulic conductivity	SWCC	HCF	Unit weight	Cohesion	Friction angle	Soil modulus	Dilation angle
	ψ_0 (kPa)	I/k_s	k_s (m/s)			γ (kN/m³)	c' (kPa)	ϕ' (°)	E_{50}^{ref} (MPa)	ψ (°)
Baseline	10	0.15	3.0×10^{-5}	SWCC-1	HCF-1	18.1	7	31.5	15	1.5
Parametric study	[5, 20]	0.15	3.0×10^{-5}	SWCC-1	HCF-1	18.1	7	31.5	15	1.5
	10	[0.02, 0.05, 0.3, 0.5][a]	3.0×10^{-5}	SWCC-1	HCF-1		7	31.5	15	1.5
	10	[0.045, 4.5][a]	$[10, 0.1] \times 10^{-5}$	SWCC-1	$\begin{bmatrix} \text{HCF-6} \\ \text{HCF-7} \end{bmatrix}$	18.1	7	31.5	15	1.5
	10	0.15	3.0×10^{-5}	$\begin{bmatrix} \text{SWCC-2} \\ \text{SWCC-3} \\ \text{SWCC-4} \\ \text{SWCC-5} \end{bmatrix}$	$\begin{bmatrix} \text{HCF-2} \\ \text{HCF-3} \\ \text{HCF-4} \\ \text{HCF-5} \end{bmatrix}$	18.1	7	31.5	15	1.5
	10	0.15	3.0×10^{-5}	SWCC-1	HCF-1	[16, 20]	7	31.5	15	1.5
	10	0.15	3.0×10^{-5}	SWCC-1	HCF-1	18.1	[0.1, 14]	31.5	15	1.5
	10	0.15	3.0×10^{-5}	SWCC-1	HCF-1	18.1	7	[25, 37]	15	1.5
	10	0.15	3.0×10^{-5}	SWCC-1	HCF-1	18.1	7	31.5	[5, 30]	1.5
	10	0.15	3.0×10^{-5}	SWCC-1	HCF-1	18.1	7	31.5	15	[0, 16, 31.5]

[a] Rainfall intensity $I = 16.2$ mm/h

Fig. 8 Hydraulic characteristic curves: (a.1), (b.1) SWCC and HCF of different n values, respectively; (a.2), (b.2) SWCC and HCF of different α values, respectively; (c) HCF of different k_s values


(a.1)

(b.1)

(a.2)

(b.2)

(c)
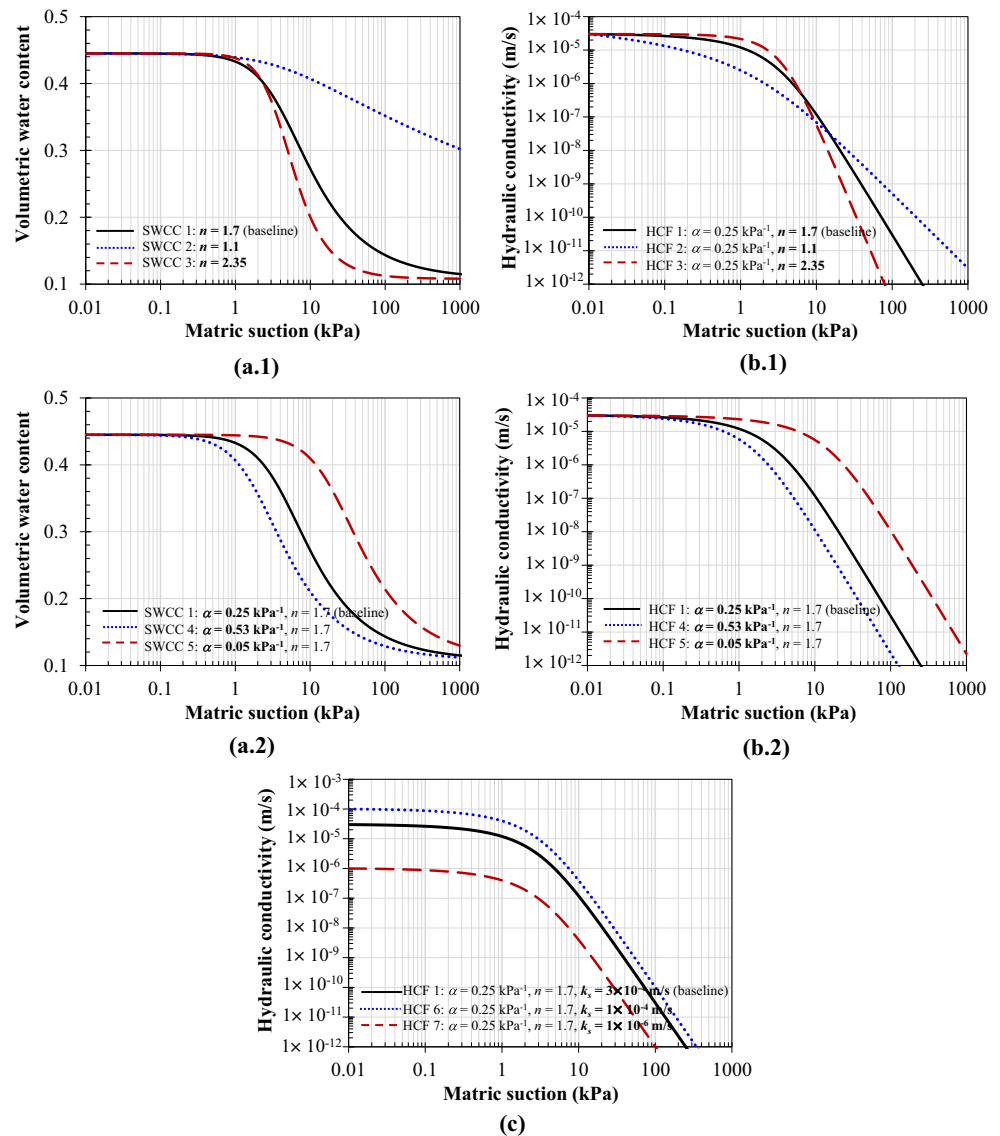
presents the variation of the PWP and VWC with time for three depths (depth-1, depth-2 and depth-3 in Fig. 7) below the slope surface at sections A, B, and C. The numerical results reveal that the development of PWP over time can be divided into four stages: the initial unsaturated stage, transition stage, temporary equilibrium stage, and development stage (inset figure in Fig. 9a). The soil was unsaturated in the initial unsaturated stage with negative PWP (or matric suction). Subsequently, the decrease of negative PWP in the transition stage was due to a loss of matric suction caused by advancement of the wetting front. As the wetting front was passed, the inflow and outflow flux tend to be balanced and the temporary equilibrium stage was achieved under a condition that negative PWP approximates were unchanged. When rainfall reached the base of the soil (at approximately $t = 21$ h), rainwater accumulated and positive PWP began to develop at the soil–bedrock interface (at $t = 24$ h) because the

permeability of the bedrock was much lower than that of the soil. At this stage (the development stage, $t > 24$ h), the PWP at the soil–bedrock interface changes from negative to positive and increases rapidly as the rainfall proceeds. It is obvious in Fig. 9 that there constantly exists a time lagging for the rapid increase in PWP for the soil at different depths because it takes some time for the PWP accumulation to reach the higher elevation. Notably, slope failure occurred at $t_f = 29$ h when the PWP at the base of the soil reached the critical threshold ($\approx$ 11 kPa), which corresponds to a PWP ratio (PWP divided by the total overburden pressure) of $r_u = 0.2$.

The VWC exhibited a similar trend over time (Fig. 9b, d, and f) to that of the PWP (Fig. 9 a, c, and e). An increase in the VWC was associated with an increase in the PWP in the transition stage. The VWC reached temporary equilibrium at $\theta = 0.39$, which corresponds to $S = 88\%$. The temporary equilibrium of the VWC is also known as the initial quasi-

Fig. 9 Variation of PWP and VWC at: **a, b** section A; **c, d** section B; **e, f** section C, with various depths below the ground surface (B-2 denotes the investigation point at depth-2 of section B)
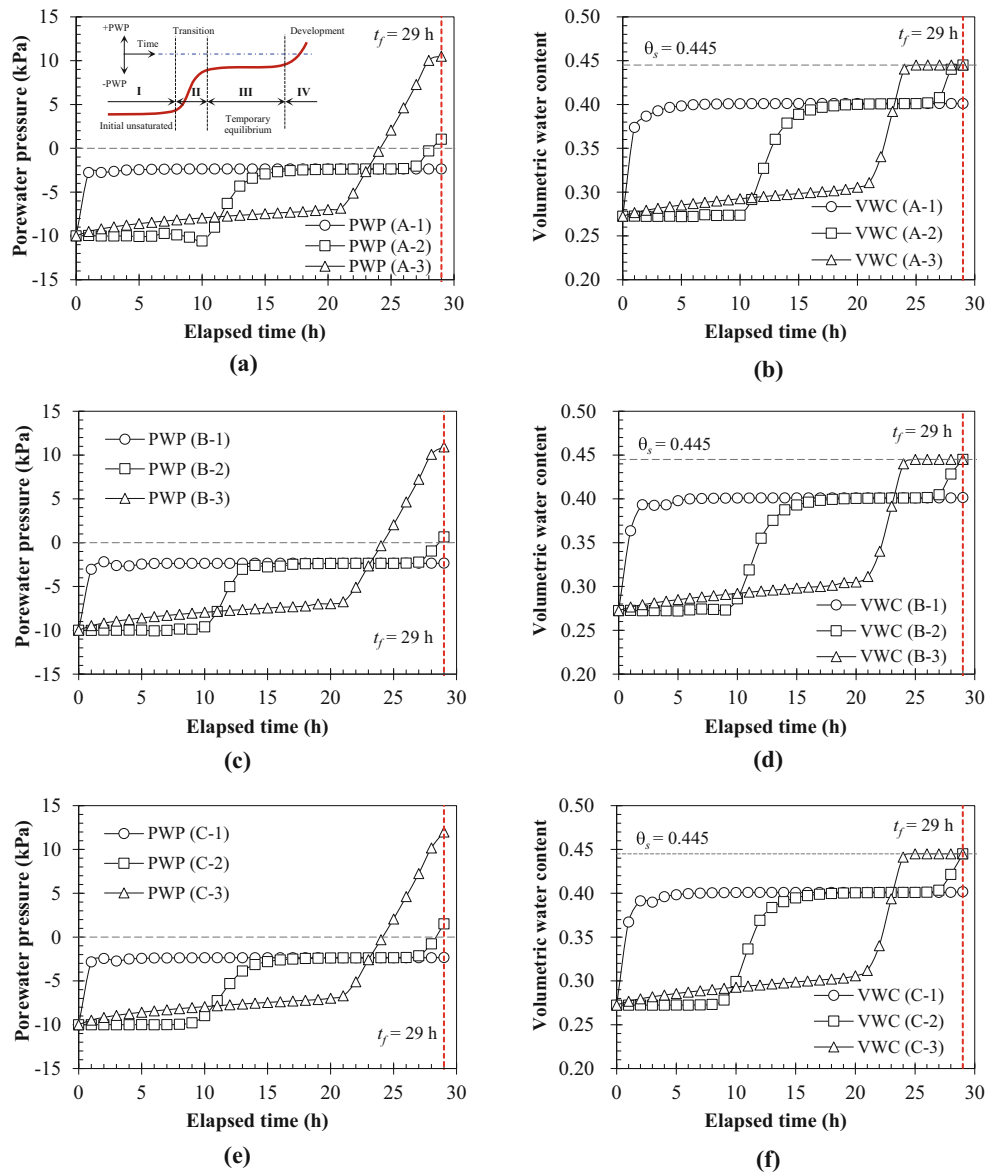
saturated VWC (Tohari et al. 2007; Ling and Ling 2012) and is an indicator used to identify the onset of slope movement. After rainfall had reached the base of the soil ($t > 21$ h), the VWC of the soil at the base increased rapidly and the soil became fully saturated ($\theta_s = 0.445$) at $t = 24$ h. Notably, in contrast to the trend of continuous increase in the positive PWP in the development stage, the VWC remained constant after the soil became saturated.

Figure 10 displays the slope total displacement over time (s–t curve) and displacement rate over time (v–t curve). The development of slope displacement was divided into three stages (the constant, accelerated, and critical deformation stages) according to the rate of slope movement, as suggested by Xu et al. (2011). Table 4 summarizes the slope displacement stage and corresponding PWP development. The slope deformation was insignificantly developed at $t < 21$ h, in

which the rainwater has not reached the base of the soil yet. The slope moved progressively with a low displacement rate ($v < 1$ mm/h) in the constant deformation stage ($21 < t < 24$ h). In this deformation stage, the PWP increased steadily but remained negative, which corresponded to the first three stages of PWP development. Subsequently, slope deformation became evident with a displacement rate ranging from $v = 1$ to 3 mm/h in the accelerated deformation stage ($24 < t < 27.2$ h). Slope deformation was triggered by full saturation of the soil and accumulation of positive PWP at the base of the soil starting from $t = 24$ h, which corresponded to the early PWP development stage (Fig. 9). The slope displacement increased rapidly with a large displacement rate ($v > 3$ mm/h) in the critical deformation stage ($t > 27.2$ h). This deformation stage corresponded to the late PWP development stage, in which the accumulation of positive PWP was larger than 7 kPa ($r_u = $

Fig. 10 Slope displacement and displacement rate with time: **a** slope displacement (s–t curve) and **b** displacement rate (v–t curve)
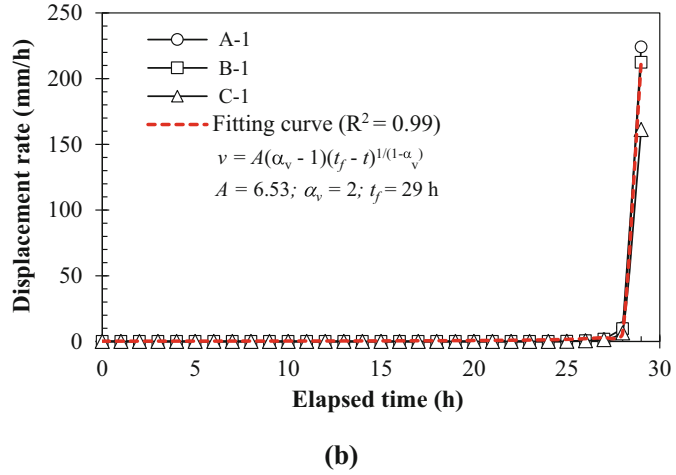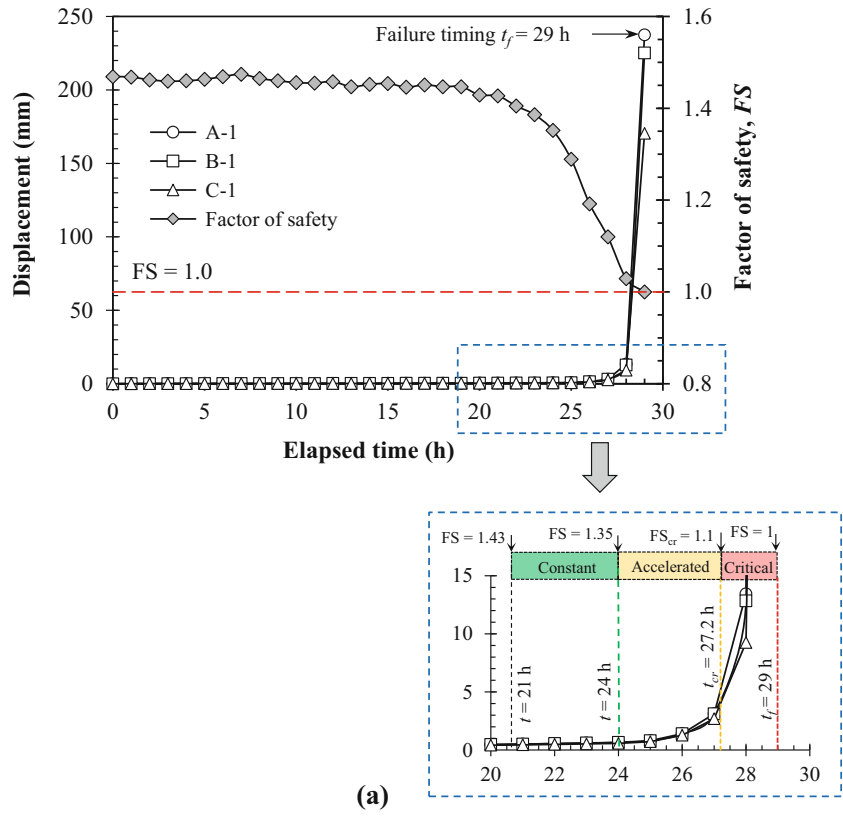

(a)

(b)

Table 4 Slope deformation and pore water pressure development in the baseline case

Slope deformation stage	Timing t (h)	Displacement rate v (mm/h)	Factor of safety (FS)	PWP development stage	PWP value (kPa)	PWP ratio r_u
Constant	21–24	< 1	1.43–1.35	Initial unsaturated, transition, and temporary equilibrium	< 0	< 0
Accelerated	24–27.2	1–3	1.35–1.1	Early development	0–7	0–0.15
Critical	27.2–29	> 3	< 1.1	Late development	7–11	0.15–0.2

Fig. 11 Location of slope failure surface in the baseline case
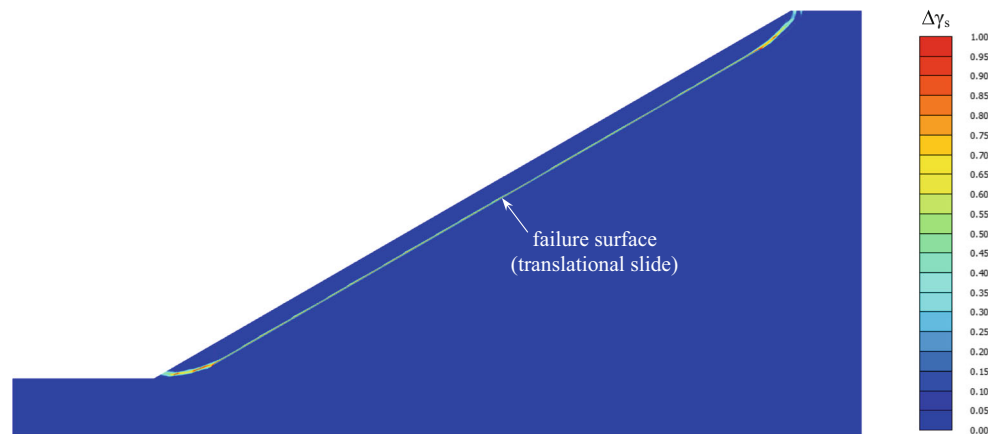
0.15). The corresponding FS at the beginning of the critical deformation stage (FS_{cr}) was 1.1. Eventually, the final slope failure (FS = 1) occurred at t_f = 29 h. The maximum slope displacement occurred in the upper slope (sections A and B) and reached 240 mm at the moment of failure (Fig. 10a).

The three stages of development of slope displacement over time can also be applied to the validation case (Fig. 4). The constant deformation stage occurred at 6000 s < t < 6700 s with a low displacement development, which corresponded to the time when the wetting front reached the base of the soil. The slope displacement then increased significantly at the accelerated deformation stage (6700 s < t < 8700 s) due to an increase in positive PWP. Finally, the slope displacement rapidly increased at the critical deformation stage until the slope failed (i.e., 8700 s < t < 9300 s). The corresponding displacement rates are also indicated in the figure.

Fukuzono's model (Fukuzono 1985) was used to fit the displacement rate versus time curve (v–t curve). The model is expressed as follows:

$$V(t) = [A(\alpha_v - 1)(t_f - t)]^{1/(1-\alpha_v)} \qquad (8)$$

where $V(t)$ = slope displacement rate (mm/h) at a given time t, t_f = the failure timing (h), and A and α_v ($\alpha_v > 1$) = fitting parameters derived by the regression. Figure 10b displays the results of fitting obtained using Fukuzono's model for the baseline case. The fitting parameters were A = 6.53 and α_v = 2, and the failure timing was t_f = 29 h. Fukuzono's model was found to fit the FE results (i.e., v–t curve) favorably with a high coefficient of determination (R^2 = 0.99). The α_v value determined in this study is consistent with the general range of α_v (between 1.6 and 2.0) reported in the literature (Intrieri et al. 2019), and the t_f value is in agreement with the predicted failure timing at FS = 1.

Figure 11 illustrates the location of the failure surface (the incremental shear strain contour). The failure surface was found to extend from the crest to the toe of the slope with the majority of the failure surface along the soil–bedrock interface. The failure mode is categorized as translational sliding failure.

Parametric study

In the parametric study, the effects of hydrological conditions and soil mechanical and hydraulic parameters on the slope displacement–time relationship were evaluated. Figure 12 presents the numerical results in terms of the s–t curves in section B-1 (middle of the slope). The slope displacement depicted in Fig. 12 was plotted only up to FS_{cr} = 1.1 (corresponding to the beginning of the critical deformation stage in the baseline case). Because the slope displacement increased considerably in the critical deformation stage, including the slope displacement in this stage would lead to indistinguishable s–t curves in the early (constant and accelerated) deformation stages. In addition, in landslide risk management, the slope displacement criterion for early warning systems is often set up according to the slope displacement value at the end of the constant or accelerated deformation stage; therefore, the present parametric study merely focused on the slope displacement in these two stages.

Influence of hydrological conditions

Regarding the effect of initial suction (Fig. 12a), the numerical results revealed that initial suction had a significant effect on the time to reach the critical deformation stage (i.e., critical deformation timing). A high ψ_0 resulted in a large time lag for the slope to reach the critical deformation stage because soil with high ψ_0 has low unsaturated permeability prior to the rainfall; thus, it is time consuming for the rainwater to seep and reach the base of soil during rainfall. The s–t curves for different ψ_0 values were similar, which resulted in approximate slope displacement at FS_{cr} = 1.1 and displacement rate in the accelerated deformation stage. This result is in response to the effect of diminishing ψ_0 as the soil tends to be saturated in this stage. However, the numerical results also revealed that
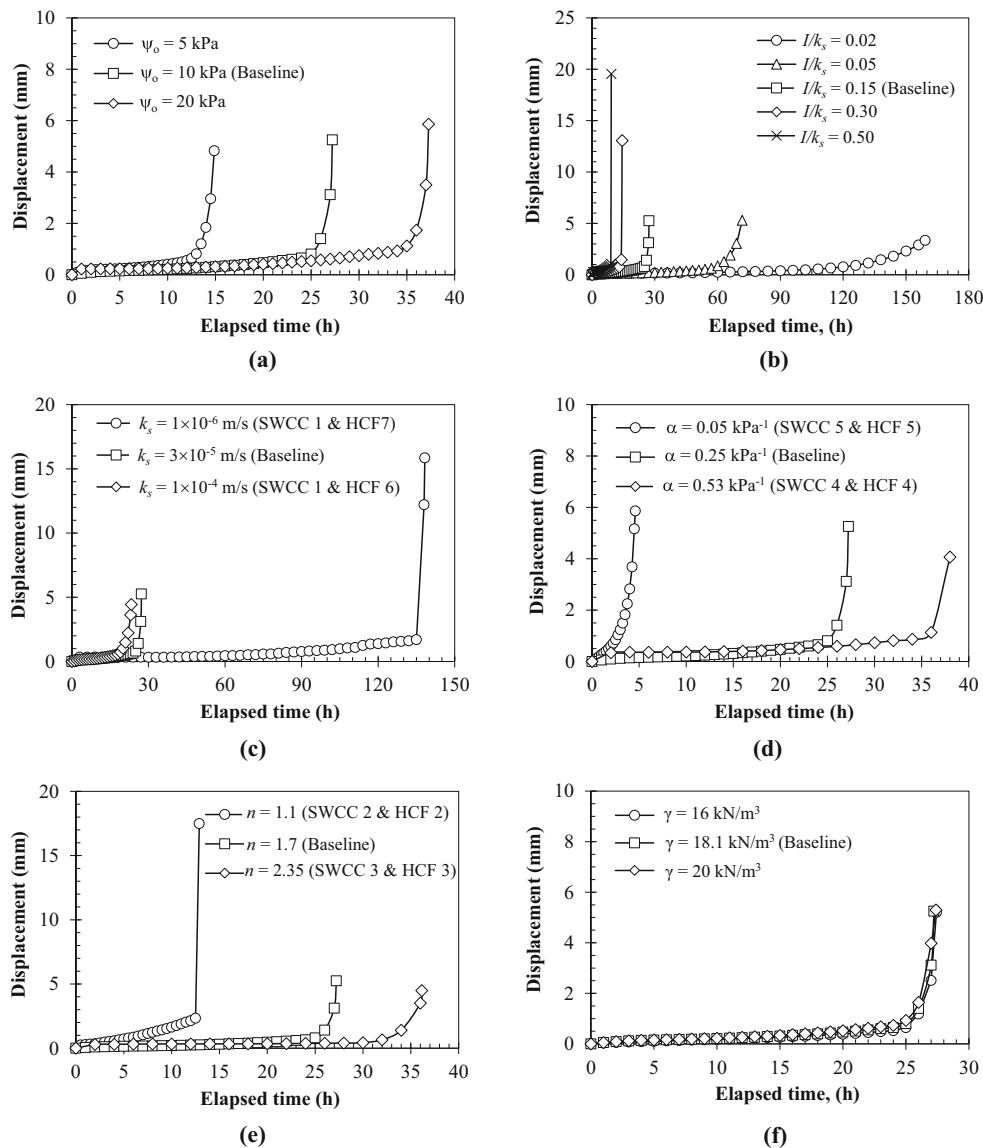
Fig. 12 Slope displacement with time in the parametric study by varying **a** initial suction, **b** I/k_s ratio, **c** saturated hydraulic conductivity, **d** fitting parameter α, **e** fitting parameter n, **f** unit weight of soil, **g** effective cohesion, **h** effective friction angle, **i** soil modulus, and **j** dilatancy angle

ψ_0 has a negligible influence on the location of the failure surface (not presented in this paper).

Regarding the influence of rainfall intensity (Fig. 12b), the numerical results indicated that rainfall intensity has a significant effect on the s–t curve. A rise of I/k_s led to critical deformation timing occurring faster and also an increase in the displacement magnitude and rate. The numerical results also indicated that the slope failure mode changed from progressive failure at low I/k_s (i.e., light and moderate rainfall) to sudden failure at high I/k_s (heavy and extremely heavy rainfall). This phenomenon is in response to the fact that the increase in PWP within the slope was a function of rainfall intensity. Intense rainfall caused rapid rainfall infiltration (or advancement of the wetting front) and hence decreased matric suction and the development of positive PWP shortly.

Figure 13 displays the location of the failure surface (indicated by the incremental shear strain contour) for different I/k_s values. The numerical results revealed that I/k_s affected the location of the failure surface. This surface mainly developed in the lower half of the slope (i.e., partial sliding failure) when the rainfall intensity was low ($I/k_s = 0.02$ in Fig. 13a), whereas it extended through the entire slope (i.e., overall sliding failure) when the rainfall intensity was moderate to high ($I/k_s = 0.15$ in Fig. 11 and $I/k_s = 0.5$ in Fig. 13b). The inconsistency of the failure surface locations is attributed to the dissimilarity of the PWP distribution within the slope, which was caused by the different rainfall intensity. In the case of low I/k_s, the time to reach critical deformation was relatively long, which allowed the rainfall-induced seepage flow driven by gravity to travel downward along the soil–bedrock interface and
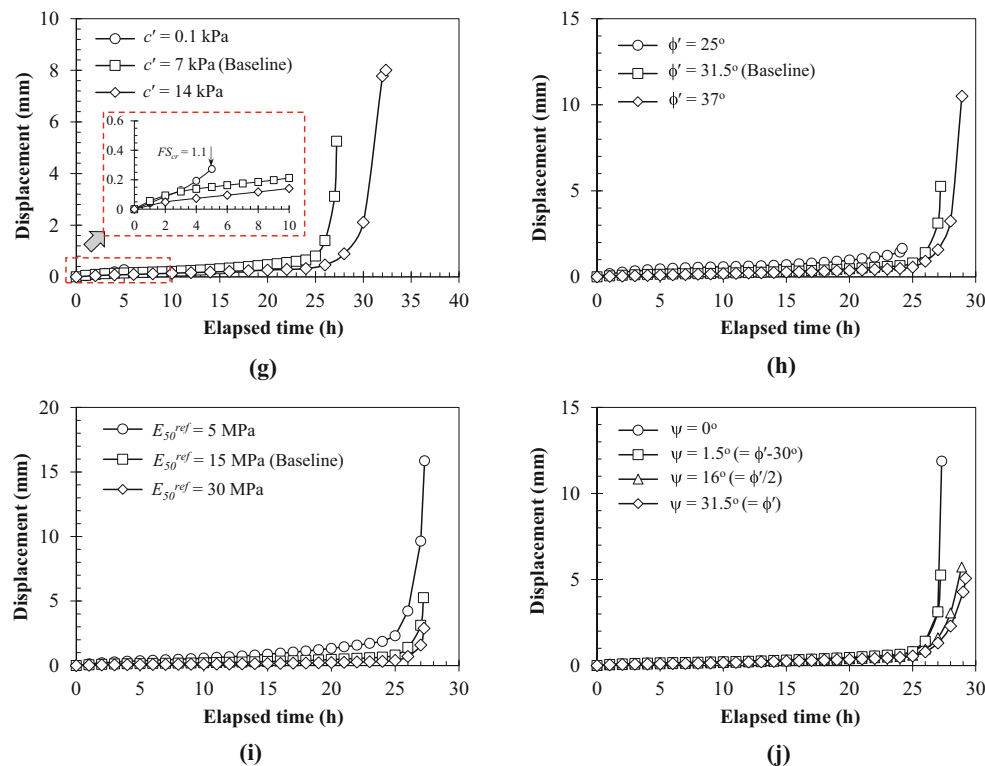
Fig. 12 (continued)

accumulate at the toe of the slope. Consequently, the PWP distribution turned into nonuniform within the slope. Specifically, a considerable increase in the PWP was observed near the slope toe. Slope failure thus occurred in the lower part of the slope as the aforementioned case.

Influence of soil hydraulic parameters

Regarding the effect of saturated hydraulic conductivity (Fig. 12c), the numerical results indicated that the critical deformation timing substantially lengthened as the soil saturated hydraulic conductivity decreased. Soil with low k_s has low permeability; therefore, it takes a long time for rainwater to infiltrate down to the base of the soil. Moreover, the slope displacement at $FS_{cr} = 1.1$ increased as k_s decreases. This slope displacement trend is associated with the development of the failure surface. The failure mode changed from shallow at high k_s to deep failure along the soil–bedrock interface at low k_s. As the k_s decreases, the failure surface developed deep within the slope due to the long duration of infiltration and seepage of rainwater prior to the critical deformation stage. Consequently, the deep failure surface for the case with low k_s could generate large slope displacement.
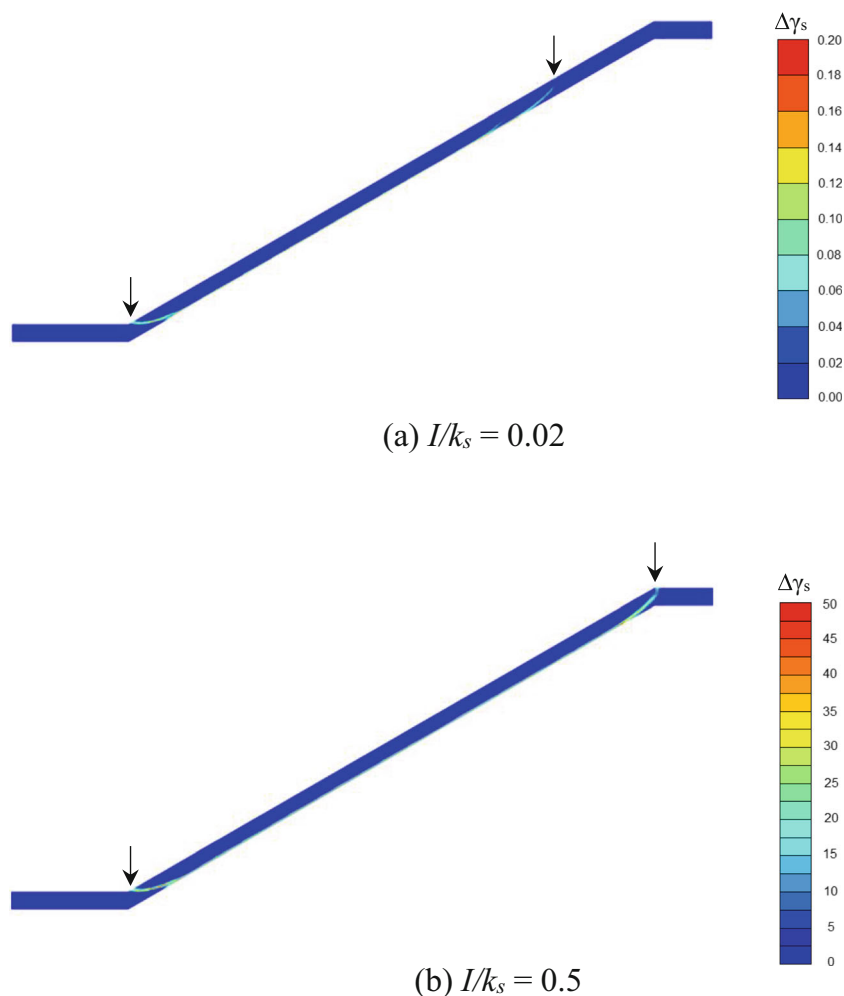
Regarding the influence of soil hydraulic characteristics under unsaturated conditions (Fig. 12d and 1e), the numerical results revealed that the SWCC and HCF influenced both the critical deformation timing and displacement rate in the accelerated deformation stage. Slopes with low α exhibited short and rapid deformation (i.e., short critical deformation timing and high displacement rate), whereas the opposite effect was observed for n. The explanation for this result is as follows. In the SWCC, α controls the air entry value (i.e., the inflection point of the SWCC) and n determines the rate of water extraction from the soil (i.e., the slope of the SWCC). For a given matric suction value lower than ψ_0, the soil unsaturated hydraulic conductivity increases as n increases (Fig. 8(a.2)) and α decreases (Fig. 8(b.2)). Consequently, soil with low α or high n has relatively high unsaturated permeability, and critical deformation occurs within a short time after the commencement of rainfall.

Influence of soil mechanical parameters

Regarding the influence of soil unit weight (Fig. 12f), the numerical results indicated that soil unit weight had a negligible effect on slope displacement. Similar s–t curves were obtained for all slope cases with different γ. The variation in VWC and the development of PWP over time were almost identical for a given investigation point for all slope cases with different γ, which resulted in comparable values of displacement magnitude, displacement rate, and critical deformation timing in the different cases. The failure in all slope cases with different γ also occurred at the same time (i.e., $t_f = 29$ h) and the same failure surface location.

Fig. 13 Effect of rainfall intensity on slope failure surface: **a** I/k_s = 0.02 and **b** I/k_s = 0.5


(a) $I/k_s = 0.02$

(b) $I/k_s = 0.5$

Regarding the influence of soil shear strength (Fig. 12g and h), the numerical results demonstrated that the critical deformation timing was strongly affected by soil cohesion but only slightly affected by the soil friction angle. The critical deformation timing increased as c' increased. For noncohesive soil (c' = 0.1 kPa), the slope reached the critical deformation stage shortly after the rainfall had begun due to the low shear strength of the soil. A shallow failure surface, typical for a noncohesive soil slope, was observed for the noncohesive soil slope case. By contrast, slope failure did not occur in the case with c' = 14 kPa. The slope remained stable (FS = 1.07) after the rainwater and seepage had reached steady-state conditions. The slope displacement at FS_{cr} = 1.1 increased as c' or ϕ' increased because in the slope with large soil shear strength, large slope displacement could develop before slope failure occurred or steady-state conditions were reached. Notably, the slope displacement rate did not significantly increase for the slope cases with low soil shear strength parameters (c = 0.1 kPa and ϕ' = 25°), which indicated that the slope with low soil shear strength could enter the critical deformation stage without exhibiting deformation features. In addition, for all slope cases of various c' or ϕ', the numerical

results revealed that the PWP distributions within the slope were similar, which suggested that the hydraulic response of the slope was independent of the soil shear strength parameters.

Regarding the influence of soil modulus (Fig. 12i), the numerical results indicated that the slope displacement at FS_{cr} = 1.1 considerably increased as the soil modulus decreased because, as expected, soil with low E_{50}^{ref} has high deformability. However, E_{50}^{ref} appeared to have little influence on the critical deformation timing and displacement rate. In addition, by inspecting the hydraulic response of the slopes, E_{50}^{ref} was discovered to have no effect on the VWC and PWP in the slope.

Regarding the influence of soil dilation angle (Fig. 12j), the numerical results revealed that the soil dilation angle affected the slope displacement magnitude and displacement rate but had only a slight effect on the critical deformation timing. The slope displacement magnitude and displacement rate increased as ψ decreased. The s–t curves for the slope cases with ψ = 16° (= $\phi'/2$) and ψ = 31.5° (= ϕ') exhibit gradual development in the accelerated deformation stage, whereas the curves for the slope cases with ψ = 0° and 1.5° exhibit sudden
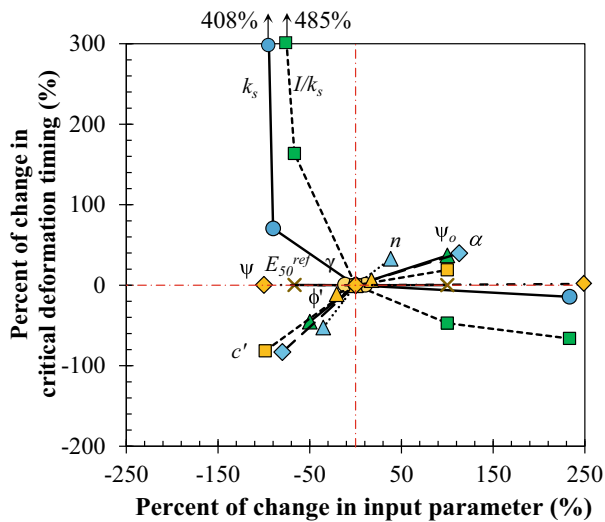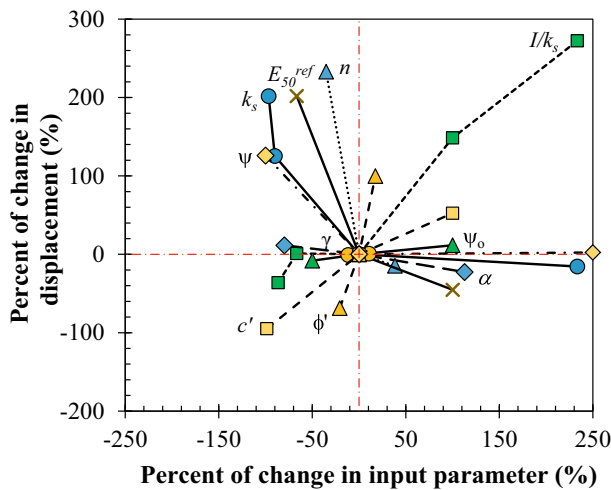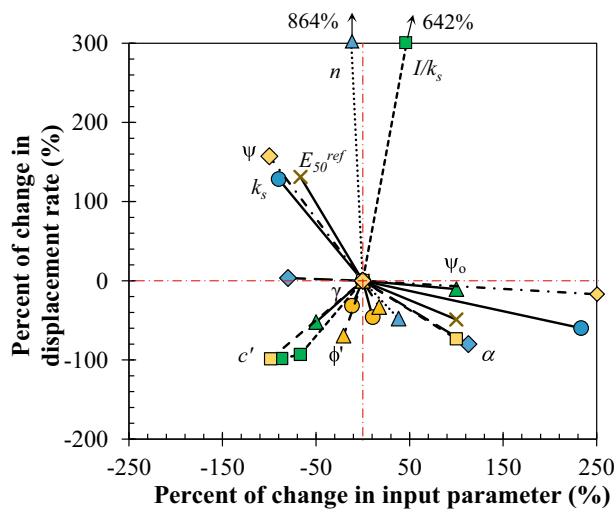
Fig. 14 Sensitivity assessment: percent of change in **a** critical deformation timing, **b** displacement, and **c** displacement rate versus percent of change in input parameters

increases. The influence of ψ on slope displacement magnitude and displacement rate can be attributed to the augment in the stiffness of the slope system with increasing ψ value, which dominates the change in volumetric plastic behavior of soil. The numerical results are consistent with the findings of Iverson (2000, 2005), who proposed an analytical model considering the effect of soil dilatancy for predicting the rate of landslide motion. Iverson found that if the soil with dense compactness in the shear zone was dilated, slow and steady landslide motion occurred when positive pore pressure was generated due to rainwater infiltration.

Sensitivity assessment

The effect of each parameter on the slope deformation characteristics was quantitatively compared in a sensitivity assessment. Figure 14 presents the results of the sensitivity assessment in terms of the percentage of change in the critical deformation timing, displacement magnitude, and displacement rate versus the percentage of change in the input parameters. In general, all the slope deformation characteristics evaluated were influenced by hydrological and geological factors. Figure 14 a indicates that ψ_0, I/k_s, k_s, α, n, and c' had a significant effect on the critical deformation timing. The hydrological conditions and soil hydraulic parameters generally had a strong influence on the critical deformation timing because these parameter groups influenced the rainfall infiltration rate and PWP development. In addition, c', the soil shear strength parameter, was directly related to slope stability and, therefore, also affected the critical deformation timing. Among the aforementioned parameters, I/k_s and k_s showed the most influential effects; the critical deformation timing increased by 485% and 408% when I/k_s and k_s were decreased by 89% and 97% on the basis of the baseline case, respectively.

Figure 14b indicates that I/k_s, k_s, n, E_{50}^{ref}, c', ϕ', and ψ had a considerable effect on the slope displacement at $FS_{cr} = 1.1$. The sensitivity assessment suggested that slope displacement was affected by the input parameters in all three parameter groups (i.e., hydrological conditions and soil hydraulic and mechanical parameters). Among these parameters, I/k_s, k_s, n, and E_{50}^{ref} had the most influential effects; the slope deformation increased by 272%, 202%, 233%, and 202% when I/k_s was increased by 233%, whereas k_s, n, and E_{50}^{ref} decreased by 97%, 35%, and 200% on the basis of the baseline case, respectively.

Figure 14c indicates that I/k_s, k_s, α, n, E_{50}^{ref}, c', ϕ', and ψ had considerable effects on the average slope displacement rate in the accelerated deformation stage. Similar to the findings for slope displacement, the slope displacement rate was affected

Fig. 15 Relationships between (a) displacement and FS and (b) displacement rate and FS

(a.1)

(b.1)

(a.2)

(b.2)

(a.3)

(b.3)
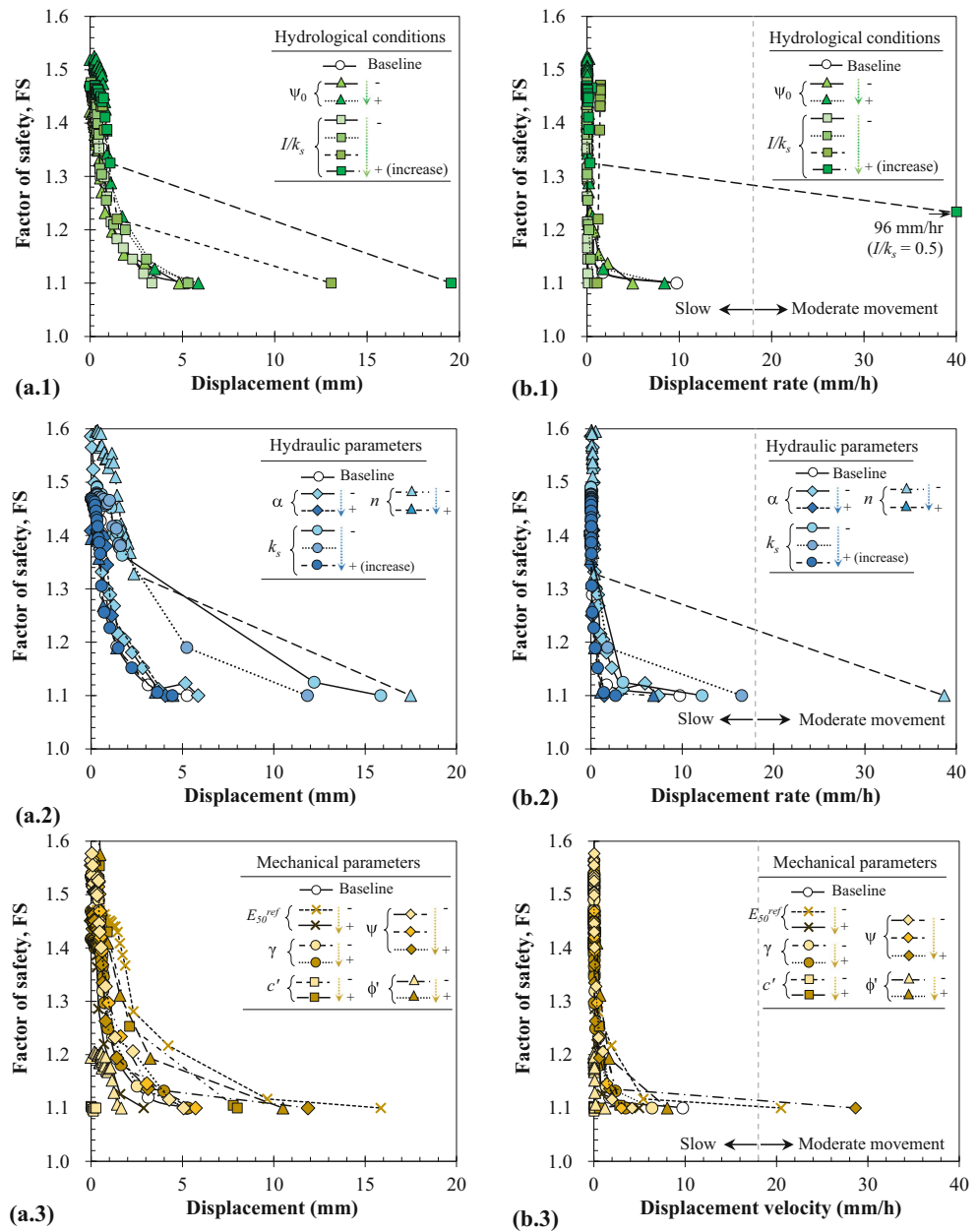
by the input parameters in all three parameter groups. The parameters I/k_s, k_s, n, and ψ had the most influential effects; the displacement rate increased by 624%, 128%, 864%, and 157% when I/k_s was increased by 100%, whereas k_s, n, and ψ decreased by 90%, 35%, and 100% on the basis of the baseline case, respectively.

In summary, the slope deformation characteristics are highly sensitive to the hydrological condition I/k_s and the hydraulic parameters k_s and n, which show great influences on the numerical calculation of critical deformation timing, slope displacement at $FS_{cr} = 1.1$, and slope displacement rate.

Slope deformation with FS

The relationships of slope displacement magnitude and displacement rate with the FS were established using the numerical data obtained from the parametric study. The relationships allow the interpretation of the slope stability level according to the monitored slope displacement information. Figure 15(a) displays the nonlinear relationship between slope displacement and the FS for different parameter groups. The displacement–FS relationship was consistent at FS > 1.3 but began to diverge at FS < 1.3 for various input parameters. As illustrated in Fig. 15(a), I/k_s, k_s, n, E_{50}^{ref}, and ψ had the strongest
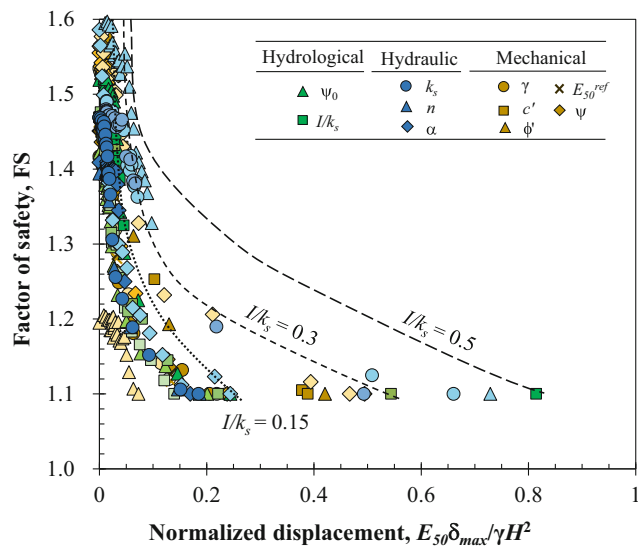
Fig. 16 Normalized displacement versus FS for normalized rainfall intensity I/k_s with different levels

Fig. 17 Regression results for displacement rate and FS relationships under different parameter groups

influences on the displacement–FS relationship. For example, under heavy rainfall conditions ($I/k_s > 0.3$), the slope displacement increased by a factor of 3–4 at low FS. The maximum slope displacement at $FS_{cr} = 1.1$ was approximately 5–20 mm under various input parameters. These slope displacement values, corresponding to landslide timing at the beginning of the critical deformation stage, can be used as criteria for providing early warning and alert before the occurrence of a landslide.

Figure 16 displays the relationship between the normalized displacement and FS for all slope cases. The normalized displacement was defined as $E_{50}\delta_{max}/\gamma H^2$, where E_{50} = secant modulus corresponding to the 50% stress level, δ_{max} = maximum displacement at the slope surface, γ = soil unit weight, and H = thickness of the residual soil. Because the displacement was only normalized using the soil mechanical parameters, the normalized displacement–FS relationship, especially for FS < 1.3, still had a wide range under different hydraulic conditions and soil hydraulic parameters. This study suggests that the normalized displacement of the slope can be further divided into three zones according to the I/k_s values (Fig. 16). In the first zone, the normalized displacement at $FS_{cr} = 1.1$ is less than 0.25 at $I/k_s < 0.15$. The majority of slope cases fell within this zone, and this finding is supported by Hearman and Hinz (2007). In their study, they concluded that low rainfall

intensity (i.e., $I/k_s < 0.2$) is insufficient to saturate soil; consequently, the surface displacement under this condition is not much different. In the second zone, the normalized displacement at $FS_{cr} = 1.1$ ranged from 0.25 to 0.55 at I/k_s of 0.15–0.3. Some soil mechanical parameters were discovered to still have influence in this zone. For the third zone, the normalized displacement at $FS_{cr} = 1.1$ varied from 0.55 to 0.80 at I/k_s of 0.3–0.5. In this zone, the normalized displacement–FS relationship was mainly influenced by the rainfall intensity and soil hydraulic parameters.

Figure 15 (b) illustrates the relationship between the displacement rate v and FS for the different parameter groups. The majority of slope cases fell within $v \leq 10$ mm/h at $FS_{cr} = 1.1$; however, v could significantly increase under some input parameters. Similar to the results for slope displacement, I/k_s, k_s, n, E_{50}^{ref}, and ψ had the strongest effects on the displacement rate–FS relationship. For example, under extremely heavy rainfall conditions ($I/k_s = 0.5$), the displacement rate increased considerably over 10 mm/h at $FS_{cr} = 1.1$, which implied that a rapid landslide could occur under high rainfall intensity.

The following hyperbolic function is proposed to describe the displacement rate–FS relationship:

$$v(t) = \frac{v_0 \times FS}{FS - FS_{cr}} \qquad (9)$$

where v(t) = displacement rate (mm/h), v_0 = constant in the hyperbolic function representing the initial value of velocity, and FS_{cr} = critical factor of safety (= 1.1 in this study). The proposed hyperbolic equation can predict the rapid increase in displacement rate as the slope approaches the critical deformation stage (i.e., FS ≈ FS_{cr}). Table 5 lists the ranges of v_0 in Eq. 9 for different parameter groups. The parameter v_0 had the widest range (up to 0.47 mm/h) under the influence of

Table 5 Regression results for displacement rate and FS relationships

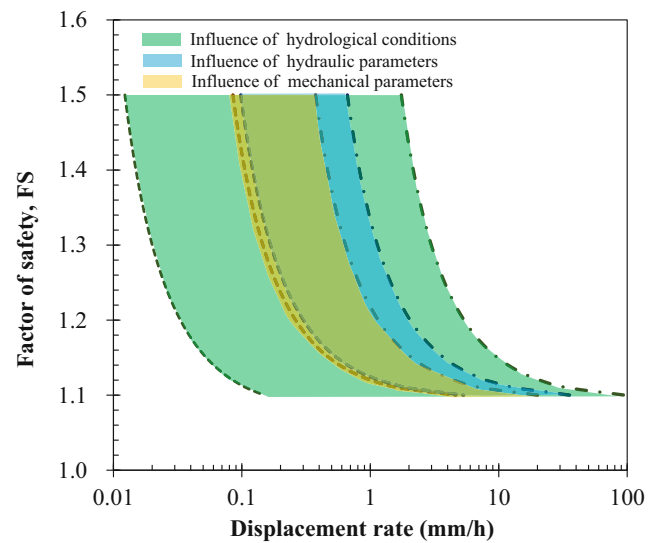| Parameter group	Range of v_0 (mm/h)	R^2
Hydrological conditions	0.0035–0.4715	0.986–0.992
Soil hydraulic parameters	0.0265–0.1793	0.892–0.991
Soil mechanical parameters	0.0230–0.1014	0.988–0.991

hydrological conditions compared with other parameter groups. Figure 17 depicts the regression results of the displacement rate–FS relationships using Eq. 9 for the different parameter groups (i.e., hydrological condition and soil hydraulic and mechanical parameters). The influence of hydrological conditions (i.e., the green color zone) caused the widest range in the displacement rate–FS relationship, followed by the influence of soil hydraulic and soil mechanical parameters. The wide range of influence of hydrological conditions can be mainly attributed to the variation in rainfall intensity considered in this study.

An additional parametric analysis was performed on a 5-m-thick soil layer to evaluate the influence of the soil thickness on the hydraulic response and slope displacement. The result of the additional parametric study (not shown in the figure) revealed that the timing of wetting front advancement and the timing of slope failure increased substantially as the soil layer becomes thicker. However, the soil thickness only has a minor effect on the positive PWP accumulation, slope displacement, displacement rate, and failure mode. Consequently, the soil thickness also has a minor effect on the relationship between FS and displacement rate.

Practical implications

The model validation results indicated that fully coupled hydro-mechanical analysis can predict the deformation characteristics and failure mode of shallow slopes subjected to rainfall with accuracy. For effective landslide risk management, coupled hydro-mechanical analyses with comprehensive site investigation can be conducted on specific slopes with high potential of landslides that would jeopardize human life and estate of residential community. The numerical results from coupled analyses provide a valuable reference for identifying the variations of PWP (or matric suction) and VWC, slope deformation characteristics, and slope stability level. Disaster prevention and mitigation strategies, such as setting up an early warning system and evacuation plan or design and construction of engineering remedial measures, can be implemented on the basis of the numerical results of FE coupled analyses.

The baseline case results indicate that slope deformation occurs in the accelerated deformation stage when the soil is fully saturated and the PWP is positive at the base of the soil. Subsequent slope failure is triggered by the positive PWP reaching a critical threshold. For field monitoring and instrumentation, measured PWP and VWC values can be indicators of slope stability level. However, in contrast to the trend of continuous increase in the positive PWP, the VWC remained constant after the soil became saturated. Consequently, compared with the VWC, the PWP may be a more suitable

indicator of slope stability after soil saturation in the later stages (i.e., the acceleration and critical deformation stages).

The parametric study and sensitivity assessment indicate that the slope deformation characteristics, namely the critical deformation timing, displacement magnitude, and displacement rate, are influenced by various hydrological and geological factors. It is found that for practical application and operation in landslide risk management, the use of a single value for the slope displacement criterion in an early warning system for all slope cases is inappropriate and irrational. Further study is required to develop a slope displacement criterion with customized values for slopes with different hydrological and geological conditions.

This study found that the relationship between slope deformation and the FS is not unique for all slope cases. The displacement–FS relationship was consistent at $FS > 1.3$ but began to diverge at $FS < 1.3$ under various input parameters. Meanwhile, a similar trend was also observed for the displacement rate–FS relationship. Conclusively, among all the input parameters, rainfall intensity (I/k_s) had the most influential effect on the aforementioned relationships. On the basis of this finding, this study proposes that the displacement–FS and displacement rate–FS relationships can be divided into several types according to the I/k_s value, as illustrated in Fig. 16. In addition, incorporating slope displacement information with PWP and VWC measurement is suggested for engineering practice to reduce the uncertainty in interpreting the slope stability level from the monitored slope displacement information. Furthermore, the suggested approach offers a comprehensive understanding of the relationship between slope deformation and stability level.

Conclusions

This study performs a series of fully coupled hydro-mechanical analyses to investigate the hydraulic response, failure mechanism, and deformation characteristics of slopes subjected to rainfall infiltration. The effects of hydrological and geological factors on slope deformation characteristics under rainfall were evaluated. The effects of each factor on the timing, magnitude, and rate of slope displacement prior to landslide occurrence were quantitatively compared through a systematic sensitivity assessment. The following conclusions were drawn according to the numerical results:

1. The numerical model validation procedures demonstrated that the fully coupled hydro-mechanical analysis based on the framework of unsaturated soil mechanics can effectively capture the mechanical and hydraulic responses and

deformation characteristics of shallow slopes subjected to rainfall. The locations of the phreatic surface and failure surface, ground surface displacement, and slope failure timing of prediction are in good agreement with those of measurement.

2. The baseline case results revealed that slope deformation is highly correlated with PWP development as rainfall lasting. Slope failure is triggered by full saturation of the soil and accumulation of positive PWP at the soil–bedrock interface. The failure surface develops along the soil–bedrock interface, and the failure type can be categorized as a translational slide failure.

3. The development of slope displacement over time can be divided into three stages, namely the constant, accelerated, and critical deformation stages, according to the rate of slope movement. In the constant deformation stage, the slope gradually moves with a low displacement rate ($v <$ 1 mm/h) and the PWP remains negative. In the accelerated deformation stage, slope deformation increases with a displacement rate ranging from 1 to 3 mm/h and the PWP becomes positive at the base of the soil. In the critical deformation stage, the displacement increases rapidly with a large displacement rate ($v > 3$ mm/h) when the positive PWP reaches a critical threshold.

4. The trend of the slope displacement rate over time can be accurately expressed using Fukuzono's model. The determined α_v (= 2.0) is consistent with the general range of α_v reported in the literature (= 1.6–2.0), and the determined t_f (= 29 h) agrees with the failure timing at FS = 1 predicted in the FE analysis.

5. The parametric study and sensitivity assessment results suggest that the slope deformation characteristics, namely the critical deformation timing, displacement magnitude, and displacement rate, are influenced by various hydrological and geological factors. The parameters I/k_s and k_s have the most influential effects on the critical deformation timing; on the other hand, I/k_s, k_s, n, E_{50}^{ref}, and ψ have crucial effects on the slope deformation magnitude and displacement rate.

6. For all slope cases, no unique relationships between slope displacement and the FS can be found in this study. The displacement–FS relationship is consistent at FS > 1.3 but begins to diverge at FS < 1.3 under various input parameters. The parameters I/k_s, k_s, n, E_{50}^{ref}, and ψ have significant influence on the displacement–FS relationship. The maximum slope displacement at $FS_{cr} = 1.1$ approximates 5–20 mm under different input parameters.

7. Regarding the displacement rate–FS relationship, the majority of slope cases fall within $v \leq 10$ mm/h at $FS_{cr} = 1.1$; however, the displacement rate can considerably increase under some input parameters. The influence of hydrological conditions causes the widest variation in the displacement rate–FS relationship, and then followed by the influence of soil hydraulic and soil mechanical parameters. The proposed hyperbolic function can accurately express the displacement rate–FS relationship.

In real conditions, the rainfall intensity could change over time, and soil properties in a slope may exhibit spatial variability. The variability and uncertainty of the hydrological condition and soil parameters are different from the uniform conditions assumed in this study. For further study, reliability analyses and probabilistic assessments are recommended to be performed in order to quantify the influence of these uncertainties on the slope deformation characteristics. Finally, the slope deformation results and values presented in this study are only limited to slopes subject to rainfall. Slope displacement induced by other loading excitations, such as soil creep, toe excavation due to engineering construction, and seismic loading, may result in different displacement magnitudes and rates. These conditions are not included in the present study.

Notation Basic SI units are given in parentheses A, empirical parameters in Fukuzono's model (dimensionless); c', effective cohesion (kPa); E_{50}, undrained soil moduli at 50% of stress level (kPa); E_{50}^{ref}, reference modulus (kPa); E_{oed}^{ref}, tangent oedometer loading modulus (kPa); E_{ur}^{ref}, unloading–reloading modulus (kPa); E_u, undrained Young's modulus (kPa); H, thickness of soil (m); I, rainfall intensity (mm/h); k, unsaturated hydraulic conductivity (m/s); k_{rel}, relative hydraulic conductivity (dimensionless); k_s, saturated hydraulic conductivity (m/s); L, length of the slope (m); m, modulus exponent (dimensionless); n, fitting parameter for van Genuchten equations (dimensionless); p^{ref}, reference confining pressure (i.e., 101.3 kPa); q, input infiltration flux (mm/h); R, correlation coefficient (dimensionless); R_f, failure ratio (dimensionless); r_u, pore water pressure coefficient (dimensionless); S, degree of saturation (%); S_e, effective saturation (%); S_r, degree of saturation at residual state (%); S_s, degree of saturation at fully saturated state (i.e., 100%); s, surface displacement (mm); t, time (h); t_f, time to slope failure (h); t_{cr}, timing corresponds to FS = 1.1 (h); u, pore water pressure at the slope base (kPa); u_a, pore air pressure (kPa); u_w, pore water pressure (kPa); v, velocity (mm/h); v_0, the initial value of velocity (mm/h); α, fitting parameter for van Genuchten equations (kPa^{-1}); α_v, empirical parameter in Fukuzono's model (dimensionless); β, slope inclination (°); ϕ, friction angle (°); ϕ', effective friction angle (°); γ, unit weight of the soil (kN/m^3); γ_{sat}, saturated soil weight below the phreatic level (kN/m^3); γ_{unsat}, unsaturated soil weight above the phreatic level (kN/m^3); γ_w, unit weight of water (kN/m^3); δ_{max}, maximum displacement at slope surface (mm); M, mean value of samples; Θ, normalized volumetric water content (dimensionless); θ, volumetric water content (dimensionless); θ_s, saturated volumetric water content (dimensionless); θ_r, residual volumetric water content (dimensionless); σ, total stress (kPa); σ', effective stress (kPa); σ_3', effective minor principal stress (kPa); σ_n, total normal stress (kPa); $(\sigma - u_a)$, net normal stress (kPa); τ, soil shear strength (kPa); ν_u, undrained Poisson's ratio (dimensionless); χ, suction coefficient (dimensionless); ψ, soil dilation angle (°); ψ_0, initial soil suction (kPa)

Appendix

Table 6 Landslide database from the literature

ID	References	Location/country	H (m)	β (°)	USCS	θ_s	θ_r	α (kPa^{-1})	n	k_{sat} (m/s)	γ (kN/m³)	c' (kPa)	ϕ' (°)
1	Bong and Son (2018)	Gyeonggi-do/Korea	2.8	31	Weathered soil (SM, SC)	0.412	0.1	0.029	1.532	1.64×10^{-6}	17.51	14.7	17.9
2	Kim et al. (2017)	Seoul/Korea	1.5~4.5	26~30	Silty sand (SM)	0.5	0.18	0.088	1.35	8×10^{-6}	18.0	11.7	25.3
3	Leshchinsky et al. (2015)	Yumokjeong landslide/Korea	5~8.5	30	Well-graded sand (SW)	n/a	n/a	0.02	1.2	5×10^{-5}	14	15	20
4	Oh and Lu (2015)	Hadong and Pohang/Korea	5.0~20	40~45	Residual soil (SW)	0.282	0	0.044	1.37	5.6×10^{-6}	17.41	0	34.1
					Mudstone and shale (MH)	0.398	0.12	0.036	1.10	3.46×10^{-6}	18.03	0	31.6
5	Song et al. (2016)	Gangwon/Korea	2.0	35	Well-graded sand (SW)	0.42^{d} / 0.40^{w}	0.067^{d} / 0.067^{w}	0.23^{d} / 0.40^{w}	2.08^{d} / 2.12^{w}	n/a	17.7	9.3	34.6
6	Oh et al. (2012)	Seochang/Korea	n/a	n/a	Clayey sand (SC)	0.388	0.012	0.090	1.366	n/a	19.78	4.5	37
		Okcheon/Korea			Poorly graded sand (SP)	0.359	0	0.115	1.282		20.38	18.6	35.3
		Yeonki/Korea				0.287	0.01	0.231	1.234		21.15	13.5	39.3
7	Dahal et al. (2009)	Shikoku/Japan	0.7~1.1	32~44	Colluvium	n/a	n/a	n/a	n/a	4.86×10^{-5}	18.2	4.9	31.5
8	Acharya et al. (2016)	Shikoku Island/Japan	0.75	31	Silty sand (SM)	0.472	n/a	n/a	n/a	2.51×10^{-7}	16.66	0.81	34.4
9	Matsushi and Matsukura (2007)	Boso Peninsula/Japan	1.2~1.8	38.8	Sandstone	0.47	0.16	1.0	2.273	6.0×10^{-5}	n/a	35.8	28.3
			2~6	26	SP-ML-CL	0.38	0.1	0.5	1.41	2.76×10^{-4}	19.5	6	27
10	Yang et al. (2017)	Taipei City/Taiwan	4~11.5	27	Mudstone	0.45	0.067	0.2	1.41	5.5×10^{-5}	21.58	16.4	17
11	Hung et al. (2018)	Kaohsiung City/Taiwan	24	28	Colluvium (clayey sandy silt)	0.39	0.057	0.081	5.239	4.8×10^{-5}	n/a	10	38
12	Ng and Shi (1998)	Seymour/Hong Kong	2.0~3.0	30	Colluvium	n/a	n/a	n/a	n/a	n/a	n/a	0.3	35.2
13	Leung and Ng (2016)	Tung Chung/Hong Kong	5.0	12~32	Colluvium (CL)	0.409^{d} / 0.394^{w}	0.049^{d} / 0.192^{w}	0.8^{d} / 1.2^{w}	1.2^{d} / 1.5^{w}	4.6×10^{-5} / $\sim 4.8 \times 10^{-6}$	n/a	25	24.8
14	Wang et al. (2017)	Shuping landslide/China	5.0	12~32	Sandstone	0.4	0.038	0.08	n/a	7.52×10^{-6}	19.5	12	30
15	Tian et al. (2016)	Hubei/China	n/a	n/a	Sandy silt	0.4	2×10^{-4}	0.902	1.3	5.0×10^{-4}	18.9	0	33.1
16	Nguyen et al. (2018)	Nakornnayok/Thailand	2.5~3.5	26	Silty (MH-ML)	0.473	0.25	0.265	1.101	2.9×10^{-5}	17.61	8.7	38.6
17	Jotisankasa and Mairaing (2010)	Chantaburi/Thailand	1.0~2.0	25~50	Silty sand (SM)	0.40	n/a	0.013	1.60	1.5×10^{-5}	n/a	1	35
18	Rahim (2016)	Putrajaya/Malaysia	10	27	Sandy silt	n/a	n/a	n/a	1.092	8.0×10^{-7}	18.0	12	18
19	Muntohar et al. (2013)	Kulonprogo/Indonesia	n/a	n/a	Silty gravel (GM)	0.48	n/a	n/a	n/a	1.19×10^{-4}	17.7	0.5	32
20	Casagli et al. (2005)	Northern Tuscany/Italy	4~5	16	Clayey sand (SC)	0.40	0.164	0.108	n/a	1.0×10^{-6}	19.4	0	36.9
21	Urciuoli et al. (2016)	Monteforte Irpino/Italy	4.0	30	Silty clays (site E)	0.659	n/a	n/a	1.495	6.85×10^{-7}	n/a	0	33
22	Bordoni et al. (2015)	Oltrepò Pavese/northern Italy	1.0	30.2	Superficial	0.425^{d} / 0.395^{w}	0.01^{d} / 0.01^{w}	0.007^{d} / 0.01^{w}	1.35^{d} / 1.43^{w}	2.0×10^{-5d} / 1.0×10^{-5w}	16.7		
23	Sorbino and Nicotera (2013)	Campania/southern Italy	4.5	30	Ashy soils A	0.565	0.135	0.124	1.716	1.0×10^{-6}	15.7	5~15	32~35
					Ashy soils B	0.617	0.143	0.115	1.602	1.0×10^{-5}	13.1	0~5	36~41
24	Tofani et al. (2006)	Tuscany/Italy	1.5~5.0	55	Silty sand (SM)	n/a	n/a	n/a	1.22	8×10^{-6}	19	0	35
25	Khan et al. (2017)	Texas/USA	2.13	21.8	(CL-CH)	0.45	0.21	0.064	1.22	5.5×10^{-7}	19.66	5.75	20
26	Chen et al. (2017)	California/USA	1.0	34	Colluvium	0.50	0.19	0.08^{d} / 0.17^{w}	2.0^{d} / 2.2^{w}	3.55×10^{-7d} / 2.59×10^{-8w}	20	1.0	20
27	Chen et al. (2018)	Western North Carolina/USA	0.6~4.0	30~34	Silty sand (SM)	0.66^{d} / 0.37^{w}	0.03^{d} / 0.03^{w}	0.45^{d} / 0.50^{w}	1.22^{d} / 1.50^{w}	6.6×10^{-5d} / 4.0×10^{-5w}	n/a	1.5	34.9
28	Collins and Znidarcic (2004)	California/USA	1.4	16	Colluvium	n/a	n/a	n/a	n/a	1.4×10^{-4}	18.6	0.2	25
29	Godt and McKenna (2008)	Seattle-Tacoma/USA	1.5	32	Colluvium (SM)	0.48	0.066	0.097	2.69	1.6×10^{-6}	n/a	4.22	33.6

Table 6 (continued)

ID	References	Location/country	Slope geometry H (m)	β (°)	Soil type USCS	Hydraulic parameters θ_s	θ_r	α (kPa^{-1})	n	k_{sat} (m/s)	Mechanical parameters γ (kN/m^3)	c' (kPa)	ϕ' (°)
30	Lu et al. (2013)	Alameda County, California/USA	n/a	n/a	A20-(SM)	0.44	0.1	0.12	1.44	1.1×10^{-7}	n/a	8.8	24
					A35-(CL-ML)	0.44	0.15	0.14	1.76	5.0×10^{-7}		4.7	35
					A55-(SP)	0.45	0.07	0.1	1.70	5.0×10^{-7}		4.1	29
					B20-(SC-SM)	0.38	0.13	0.05	1.75	1.2×10^{-7}		20.3	32
					B37-(ML)	0.47	0.15	0.12	1.50	8.0×10^{-7}		12.5	35
					B62-(SM)	0.50	0.19	0.08	2.00	1.0×10^{-7}		6.6	37
31	Thomas et al. (2018)	San Francisco Bay/USA	0.75~1.5	34	Silty sand (SM) to silty clay (CL)	0.39	0.05	0.302	1.95	1.5×10^{-5}	n/a	7	33
						0.38	0.13	0.188	1.76				
						0.43	0.17	0.215	2.29				
32	Wayllace et al. (2019)	Colorado, USA	1.0~4.0	31	Tunnel fill and colluvium	0.33	0.08	0.235	2.12	5.79×10^{-6} 6.94×10^{-5}	20	0	30~34
33	Suradi et al. (2016)	Jabiru/Australia	2.0	19	Silty sand (SM)	n/a	n/a	n/a	n/a	2.22×10^{-6}	n/a	3	32
34	Cuomo and Della Sala (2013)	Japan	n/a	n/a	n/a	0.46	0.17	0.548	2.3	1.0×10^{-4}	n/a	3	32
		China				0.37	0.15	0.556	1.4	1.2×10^{-6}	n/a	n/a	33
		Thailand				0.37	0.2	0.714	1.5	1.0×10^{-5}	n/a	3	36.6
		Italy				0.66	0	0.19	1.3	1.0×10^{-5}	13.3	11.7	39.5
		Italy				0.43	0.16	0.143	1.9	1.1×10^{-6}	19.4	0	32
		Italy				0.45	0.19	0.111	1.6	1.3×10^{-6}	18.7	0.5	35
		Italy				0.50	0.18	0.111	2.1	9.26×10^{-6}	n/a	0	n/a
		USA				0.41	0.06	0.61	2.1	1.6×10^{-6}	n/a	3	33.6
		New Zealand				0.49	0.18	0.1	1.5	1.49×10^{-5}	17.6	5	30

β = angle inclination of slope; H = soil thickness; θ_s = saturated volumetric water content; n, α = fitting parameters in van Genuchten model; k_{sat} = saturated hydraulic conductivity; γ = soil unit weight; c' = effective cohesion; ϕ' = friction angle; ^{d} = the drying SWCC; ^{w} = the wetting SWCC; θ_r = residual volumetric water content; n/a = information is not available

References

Acharya KP, Bhandary NP, Dahal RK, Yatabe R (2016) Seepage and slope stability modelling of rainfall-induced slope failures in topographic hollows. Geomat Nat Haz Risk 7(2):721–746

Ahmadi-Adli M, Huvaj N, Toker NK (2017) Rainfall-triggered landslides in an unsaturated soil: a laboratory flume study. Environ Earth Sci 76(21):735

Alonso EE, Gens A, Delahaye CH (2003) Influence of rainfall on the deformation and stability of a slope in overconsolidated clays: a case study. Hydrogeol J 11(1):174–192

Bandara S, Ferrari A, Laloui L (2016) Modelling landslides in unsaturated slopes subjected to rainfall infiltration using material point method. Int J Numer Anal Met 40(9):1358–1380

Beyer W (1964) Zur Bestimmung der Wasserdurchlassigkeit von Kieson und Sanduen aus der Kornverteilung [On the determination of hydraulic conductivity of gravels and sands from grain-size distribution]. Wasserwirtsch Wassertech 14:165–169

Bhattacherjee D, Viswanadham BVS (2017) Effect of geocomposite layers on slope stability under rainfall condition. Indian Geotech J 48(2):316–326

Bishop AW (1954) The use of pore-pressure coefficients in practice. Géotechnique 4(4):148–152

Bishop AW (1959) The principle of effective stress. Teknisk Ukeblad 106(39):859–863

Bolton MD (1986) The strength and dilatancy of sands. Geotechnique 36(1):65–78

Bong T, Son Y (2018) Probabilistic analysis of weathered soil slope in South Korea. Adv Civ Eng 2018:12

Bordoni M, Meisina C, Valentino R, Lu N, Bittelli M, Chersich S (2015) Hydrological factors affecting rainfall-induced shallow landslides: from the field monitoring to a simplified slope stability analysis. Eng Geol 193:19–37

Brinkgreve RBJ, Kumarswamy S, Swolfs WM (2019) PLAXIS 2019 manual. PLAXIS bv, Delft

Caine N (1980) The rainfall intensity duration control of shallow landslides and debris flows. Geogr Ann 62(1–2):23–27

Camera CAS, Apuani T, Masetti M (2014) Mechanisms of failure on terraced slopes: the Valtellina case (northern Italy). Landslides 11(1):43–54

Casagli N, Dapporto S, Ibsen ML, Tofani V, Vannocci P (2005) Analysis of the landslide triggering mechanism during the storm of 20th–21st November 2000, in northern Tuscany. Landslides 3(1):13–21

Chae BG, Kim MI (2012) Suggestion of a method for landslide early warning using the change in the volumetric water content gradient due to rainfall infiltration. Environ Earth Sci 66(7):1973–1986

Chae BG, Lee JH, Park HJ, Choi J (2015) A method for predicting the factor of safety of an infinite slope based on the depth ratio of the wetting front induced by rainfall infiltration. Nat Hazard Earth Syst 15(8):1835–1849

Chen R-H, Kuo K-J, Chien W-N (2012) Failure mechanism of granular soil slopes under high intensity rainfalls. J GeoEng 7(1):21–31

Chen CW, Saito H, Oguchi T (2015) Rainfall intensity–duration conditions for mass movements in Taiwan. Progress in Earth and Planetary Science 2(1):14

Chen P, Mirus B, Lu N, Godt JW (2017) Effect of hydraulic hysteresis on stability of infinite slopes under steady infiltration. J Geotech Geoenviron 143(9):04017041

Chen P, Lu N, Formetta G, Godt JW, Wayllace A (2018) Tropical storm-induced landslide potential using combined field monitoring and numerical modeling. J Geotech Geoenviron 144(11):05018002

Chinkulkijniwat A, Yubonchit S, Horpibulsuk S, Jothityangkoon C, Jeeptaku C, Arulrajah A (2016) Hydrological responses and stability analysis of shallow slopes with cohesionless soil subjected to continuous rainfall. Can Geotech J 53(12):2001–2013

Cogan J, Gratchev I (2019) A study on the effect of rainfall and slope characteristics on landslide initiation by means of flume tests. Landslides, 16(12):2369–2379

Collins BD, Znidarcic D (2004) Stability analyses of rainfall induced landslides. J Geotech Geoenviron 130(4):362–372

Cuomo S, Della Sala M (2013) Rainfall-induced infiltration, runoff and failure in steep unsaturated shallow soil deposits. Eng Geol 162:118–127

Dahal RK, Hasegawa S, Nonomura A, Yamanaka M, Masuda T, Nishino K (2009) Failure characteristics of rainfall-induced shallow landslides in granitic terrains of Shikoku Island of Japan. Environ Geol 56(7):1295–1310

Fan W, Wei YN, Deng LS (2018) Failure modes and mechanisms of shallow debris landslides using an artificial rainfall model experiment on Qin-Ba mountain. Int J Geomech 18(3):04017157

Fourie AB, Rowe D, Blight GE (1999) The effect of infiltration on the stability of the slopes of a dry ash dump. Géotechnique 49(1):1–13

Fukuzono T (1985) A new method for predicting the failure time of a slope. In: Proceedings of 4th international conference and field workshop on landslides. Tokyo University Press, Tokyo, pp 145–150

Gallage C, Jayakody S, Uckimura T (2012) Effects of slope inclination on the rain-induced instability of embankment slopes. In: Zakaria M, Huat BBK (eds) Proceedings of the second international conference on geotechnique, construction materials and environment. The GEOMATE International Society, Kuala Lumpur, pp 196–201

Gasmo J, Hritzuk KJ, Rahardjo H, Leong EC (1999) Instrumentation of an unsaturated residual soil slope. Geotech Test J 22(2):134–143

Ghasemi P, Cumo S, Perna AD, Martinelli M, Calvello M (2019) MPM-analysis of lnadslide propagation observed in flume test. Proceedings of 2nd international conference on the material point method for modelling soil-water-structure interaction

Godt JW, McKenna JP (2008) Numerical modeling of rainfall thresholds for shallow landsliding in the Seattle, Washington, area. In: Baum RL, Godt JW, Highland LM (eds) Landslides and engineering geology of the Seattle, Washington, area. Geological Society of America, Boulder, pp 121–135

Griffiths DV, Lu N (2005) Unsaturated slope stability analysis with steady infiltration or evaporation using elasto-plastic finite elements. Int J Numer Anal Met 29(3):249–267

Griffiths DV, Huang JS, Dewolfe GF (2011) Numerical and analytical observations on long and infinite slopes. Int J Numer Anal Met 35(5):569–585

Hakro MR, Harahap ISH (2015) Laboratory experiments on rainfall-induced flowslide from pore pressure and moisture content measurements. Nat Hazards Earth Syst Sci Discuss 3(2):1575–1613

Hazen A (1892) Some physical properties of sands and gravels, with special reference to their use in filtration. Massachusetts State Board of Health, 24th annual report, 539–556

Hearman AJ, Hinz C (2007) Sensitivity of point scale surface runoff predictions to rainfall resolution. Hydrol Earth Syst Sci 11(2):965–982

Houston WN, Dye HB, Zapata CE, Perera YY, Harraz A (2006) Determination of SWCC using one point measurement and standard curves. In: Miller GA, Zapata CE, Houston SL, Fredlund DG (eds) Proceedings of the 4th international conference on unsaturated soils. Geotechnical special publication no. 147. American Society of Civil Engineers, Reston, pp 1482–1493

Hung C, Liu C-H, Chang C-M (2018) Numerical investigation of rainfall-induced landslide in mudstone using coupled finite and discrete element analysis. Geofluids 2018:1–15

Intrieri E, Carlà T, Gigli G (2019) Forecasting the time of failure of landslides at slope-scale: a literature review. Earth Sci Rev 193:333–349

Iverson RM (2000) Landslide triggering by rain infiltration. Water Resour Res 36(7):1897–1910

Iverson RM (2005) Regulation of landslide motion by dilatancy and pore pressure feedback. J Geophys Res-Earth 110(F2)

Jing X, Chen Y, Pan C, Yin T, Wang W, Fan X (2019) Erosion failure of a soil slope by heavy rain: laboratory investigation and modified GA model of soil slope failure. Int J Environ Res Public Health 16(6): 1075

Johnson KA, Sitar N (1990) Hydrologic conditions leading to debris-flow initiation. Can Geotech J 27(6):789–801

Jotisankasa A, Mairaing W (2010) Suction-monitored direct shear testing of residual soils from landslide-prone areas. J Geotech Geoenviron 136(3):533–537

Khan MS, Hossain S, Ahmed A, Faysal M (2017) Investigation of a shallow slope failure on expansive clay in Texas. Eng Geol 219: 118–129

Kim KS, Song YS (2015) Geometrical and geotechnical characteristics of landslides in Korea under various geological conditions. J Mt Sci 12(5):1267–1280

Kim J, Kim Y, Jeong S, Hong M (2017) Rainfall-induced landslides by deficit field matric suction in unsaturated soil slopes. Environ Earth Sci 76(23):808

Kim MS, Onda Y, Uchida T, Kim JK, Song YS (2018) Effect of seepage on shallow landslides in consideration of changes in topography: case study including an experimental sandy slope with artificial rainfall. Catena 161:50–62

Kozeny J (1927) Uber Kapillare Leitung der Wasser in Boden. R Acad Sci Vienna, Proc Class I 136:271–306

Lee LM, Kassim A, Gofar N (2011) Performances of two instrumented laboratory models for the study of rainfall infiltration into unsaturated soils. Eng Geol 117(1–2):78–89

Leshchinsky B, Vahedifard F, Koo HB, Kim SH (2015) Yumokjeong landslide: an investigation of progressive failure of a hillslope using the finite element method. Landslides 12(5):997–1005

Leung AK, Ng CWW (2013) Analyses of groundwater flow and plant evapotranspiration in a vegetated soil slope. Can Geotech J 50(12): 1204–1218

Leung AK, Ng CWW (2016) Field investigation of deformation characteristics and stress mobilisation of a soil slope. Landslides 13(2): 229–240

Li AG, Yue ZQ, Tham LG, Lee CF, Law KT (2005) Field-monitored variations of soil moisture and matric suction in a saprolite slope. Can Geotech J 42(1):13–26

Ling H, Ling HI (2012) Centrifuge model simulations of rainfall-induced slope instability. J Geotech Geoenviron 138(9):1151–1157

Lora M, Camporese M, Troch PA, Salandin P (2016) Rainfall-triggered shallow landslides: infiltration dynamics in a physical hillslope model. Hydrol Process 30(18):3239–3251

Lu N, Kaya M, Collins BD, Godt JW (2013) Hysteresis of unsaturated hydromechanical properties of a silty soil. J Geotech Geoenviron 139(3):507–510

Matsushi Y, Matsukura Y (2007) Rainfall thresholds for shallow landsliding derived from pressure-head monitoring: cases with permeable and impermeable bedrocks in Boso Peninsula, Japan. Earth Surf Process Landf 32(9):1308–1322

Milledge DG, Griffiths DV, Lane SN, Warburton J (2012) Limits on the validity of infinite length assumptions for modelling shallow landslides. Earth Surf Process Landf 37(11):1158–1166

Montoya-Domínguez J, García-Aristizábal E, Vega-Posada C (2016) Effect of rainfall infiltration on the hydraulic response and failure mechanisms of sandy slope models. Rev Fac Ing 25(43):97–109

Moriwaki H, Inokuchi T, Hattanji T, Sassa K, Ochiai H, Wang G (2004) Failure processes in a full-scale landslide experiment using a rainfall simulator. Landslides 1(4):277–288

Mualem Y (1976) A new model for predicting the hydraulic conductivity of unsaturated porous media. Water Resour Res 12(3):513–522

Muntohar AS, Ikhsan J, Liao HJ (2013) Influence of rainfall patterns on the instability of slopes. Civ Eng Dimens 15(2):120–128

Ng CWW, Shi Q (1998) A numerical investigation of the stability of unsaturated soil slopes subjected to transient seepage. Comput Geotech 22(1):1–28

Nguyen TS, Likitlersuang S, Jotisankasa A (2018) Stability analysis of vegetated residual soil slope in Thailand under rainfall conditions. Environ Geotech, 0(0), 1–12

Ochiai H, Okada Y, Furuya G, Okura Y, Matsui T, Sammori T, Terajima T, Sassa K (2004) A fluidized landslide on a natural slope by artificial rainfall. Landslides 1(3):211–219

Oh S, Lu N (2015) Slope stability analysis under unsaturated conditions: case studies of rainfall-induced failure of cut slopes. Eng Geol 184: 96–103

Oh S, Lu N, Kim YK, Lee SJ, Lee SR (2012) Relationship between the soil-water characteristic curve and the suction stress characteristic curve: experimental evidence from residual soils. J Geotech Geoenviron 138(1):47–57

Okura Y, Kitahara H, Ochiai H, Sammori T, Kawanami A (2002) Landslide fluidization process by flume experiments. Eng Geol 66(1–2):65–78

Park MC (2016) Behavior analysis by model slope experiment of artificial rainfall. Nat Hazard Earth Syst 16(3):789–800

Qi SC, Vanapalli SK (2015) Hydro-mechanical coupling effect on surficial layer stability of unsaturated expansive soil slopes. Comput Geotech 70:68–82

Rahardjo H, Lee T, Leong E, Rezaur R (2005) Response of a residual soil slope to rainfall. Can Geotech J 42(2):340–351

Rahardjo H, Melinda F, Leong EC, Rezaur RB (2011) Stiffness of a compacted residual soil. Eng Geol 120(1–4):60–67

Rahim MSM (2016) Hydro-mechanical behaviour of a residual soil slope in Malaysia. Doctoral thesis, Durham University, Durham E-Theses Online

Regmi RK, Jung K, Nakagawa H, Do XK, Mishra BK (2017) Numerical analysis of multiple slope failure due to rainfall: based on laboratory experiments. Catena 150:173–191

Sasahara K (2017) Prediction of the shear deformation of a sandy model slope generated by rainfall based on the monitoring of the shear strain and the pore pressure in the slope. Eng Geol 224:75–86

Slichter CS (1954) Theoretical investigation of the motion of ground waters. U.S. Dept. of the Interior, Geological Survey, Water Resources Division, Ground Water Branch, Washington, DC

Song YS, Chae BG, Lee J (2016) A method for evaluating the stability of an unsaturated slope in natural terrain during rainfall. Eng Geol 210: 84–92

Sorbino G, Nicotera MV (2013) Unsaturated soil mechanics in rainfall-induced flow landslides. Eng Geol 165:105–132

Suradi M, Fourie AB, Saynor MJ (2016) An experimental and numerical study of a landslide triggered by an extreme rainfall event in northern Australia. Landslides 13(5):1125–1138

Tang Y, Wu W, Yin KL, Wang S, Lei G (2019) A hydro-mechanical coupled analysis of rainfall induced landslide using a hypoplastic constitutive model. Comput Geotech 112:284–292

Thomas MA, Mirus BB, Collins BD, Lu N, Godt JW (2018) Variability in soil-water retention properties and implications for physics-based simulation of landslide early warning criteria. Landslides 15(7): 1265–1277

Tian DF, Zheng H, Liu DF (2016) A 2D integrated FEM model for surface water–groundwater flow of slopes under rainfall condition. Landslides 14(2):577–593

Tofani V, Dapporto S, Vannocci P, Casagli N (2006) Infiltration, seepage and slope instability mechanisms during the 20-21 November 2000 rainstorm in Tuscany, central Italy. Nat Hazard Earth Syst 6(6): 1025–1033

Tofani V, Bicocchi G, Rossi G, Segoni S, D'Ambrosio M, Casagli N, Catani F (2017) Soil characterization for shallow landslides modeling: a case study in the Northern Apennines (central Italy). Landslides 14(2):755–770

Tohari A, Nishigaki M, Komatsu M (2007) Laboratory rainfall-induced slope failure with moisture content measurement. J Geotech Geoenviron 133(5):575–587

Trandafir AC, Sidle RC, Gomi T, Kamai T (2008) Monitored and simulated variations in matric suction during rainfall in a residual soil slope. Environ Geol 55(5):951–961

Urciuoli G, Pirone M, Comegna L, Picarelli L (2016) Long-term investigations on the pore pressure regime in saturated and unsaturated sloping soils. Eng Geol 212:98–119

van Asch TWJ, Buma J, Van Beek LPH (1999) A view on some hydrological triggering systems in landslides. Geomorphology 30(1–2): 25–32

van Genuchten MT (1980) A closed-form equation for predicting the hydraulic conductivity of unsaturated soils. Soil Sci Soc Am J 44(5):892–898

Vanapalli SK, Fredlund DG, Pufahl DE, Clifton AW (1996) Model for the prediction of shear strength with respect to soil suction. Can Geotech J 33(3):379–392

Wang G, Sassa K (2001) Factors affecting rainfall-induced flowslides in laboratory flume tests. Geotechnique 51(7):587–599

Wang GH, Sassa K (2003) Pore-pressure generation and movement of rainfall-induced landslides: effects of grain size and fine-particle content. Eng Geol 69(1–2):109–125

Wang R, Zhang G, Zhang JM (2010) Centrifuge modelling of clay slope with montmorillonite weak layer under rainfall conditions. Appl Clay Sci 50(3):386–394

Wang DJ, Tang HM, Zhang YH, Li CD, Huang L (2017) An improved approach for evaluating the time-dependent stability of colluvial landslides during intense rainfall. Environ Earth Sci 76(8):321

Wang B, Vardon PJ, Hicks MA (2018) Rainfall-induced slope collapse with coupled material point method. Eng Geol 239:1–12

Wayllace A, Thunder B, Lu N, Khan A, Godt JW (2019) Hydrological behavior of an infiltration-induced landslide in Colorado, USA. Geofluids 2019:14

Wesley L (2011) Stability of slopes in residual soils. Obras y proyectos 10:47–61

Wu LZ, Huang RQ, Xu Q, Zhang LM, Li HL (2015) Analysis of physical testing of rainfall-induced soil slope failures. Environ Earth Sci 73(12):8519–8531

Wu LZ, Zhou Y, Sun P, Shi JS, Liu GG, Bai LY (2017) Laboratory characterization of rainfall-induced loess slope failure. Catena 150: 1–8

Xu Q, Yuan Y, Zeng YP, Hack R (2011) Some new pre-warning criteria for creep slope failure. Sci China Technol Sci 54(1):210–220

Yang KH, Uzuoka R, Thuo JN, Lin GL, Nakai Y (2017) Coupled hydro-mechanical analysis of two unstable unsaturated slopes subject to rainfall infiltration. Eng Geol 216:13–30

Ye GL, Zhang F, Yashima A, Sumi T, Ikemura T (2005) Numerical analyses on progressive failure of slope due to heavy rain with 2D and 3D FEM. Soils Found 45(2):1–15

Yubonchit S, Chinkulkijniwat A, Horpibulsuk S, Jothityangkoon C, Arulrajah A, Suddeepong A (2017) Influence factors involving rainfall-induced shallow slope failure: numerical study. Int J Geomech 17(7):04016158

Zhang J, Jiao JJ, Yang J (2000) In situ rainfall infiltration studies at a hillside in Hubei Province, China. Eng Geol 57(1–2):31–38

Zhang G, Qian JY, Wang R, Zhang JM (2011) Centrifuge model test study of rainfall-induced deformation of cohesive soil slopes. Soils Found 51(2):297–305

Zhang LL, Fredlund DG, Fredlund MD, Wilson GW (2014) Modeling the unsaturated soil zone in slope stability analysis. Can Geotech J 51(12):1384–1398

Zhang S, Xu Q, Zhang Q (2017) Failure characteristics of gently inclined shallow landslides in Nanjiang, southwest of China. Eng Geol 217: 1–11

Zhang S, Zhang X, Pei X, Wang S, Huang R, Xu Q, Wang Z (2019) Model test study on the hydrological mechanisms and early warning thresholds for loess fill slope failure induced by rainfall. Eng Geol 258:105–135

Zhou YD, Cheuk CY, Tham LG (2009) Deformation and crack development of a nailed loose fill slope subjected to water infiltration. Landslides 6(4):299–308